



14

## Abstract

15 The oxidation state of Ge in silicate glasses, quenched from melts, was determined by X-ray  
16 absorption spectroscopy. The melts were equilibrated over the range of relative oxygen  
17 fugacities ( $fO_2$ ) from IW -3 to IW +10, where IW is the iron-wüstite oxygen buffer in  
18 logarithmic units. X-ray absorption near edge structure (XANES) spectra of the samples  
19 show that over the range in  $fO_2$  from IW -2.8 to IW +2.4, the  $Ge^{4+}/(Ge^{2+} + Ge^{4+})$  ratio  
20 increases from 0.05 to 0.95. Modelling of extended X-ray absorption fine structure (EXAFS)  
21 gives the  $Ge^{2+}$ -O bond length as  $1.89 \pm 0.03 \text{ \AA}$ . Olivine-melt partitioning experiments were  
22 also conducted, which show that  $Ge^{2+}$  is highly incompatible, with  $D_{Ge^{2+}}^{ol/melt} < 0.005$ , whereas  
23  $D_{Ge^{4+}}^{ol/melt}$  is  $\sim 1$ , where D is the partition coefficient. The geochemical properties of Ge during  
24 the magmatic differentiation of the Moon and other reduced rocky planets and achondrite  
25 parent bodies will therefore be entirely different to that familiar from terrestrial examples. In  
26 particular, the incompatible nature of  $Ge^{2+}$  may explain the anomalous enrichment of Ge in  
27 KREEP basalts.

28

## 29 Keywords

30 Germanium, silicate melt, oxidation state, XANES, EXAFS, partitioning

31

32

## 33 1 Introduction

34 Germanium typically occurs as a 4+ cation,  $\text{Ge}^{4+}$ , behaving like  $\text{Si}^{4+}$  in minerals and melts in  
35 the Earth's crust and upper mantle (Bernstein, 1985). Partial melting and crystallisation cause  
36 little fractionation of Ge, so the concentration of Ge is quite homogeneous at 1–2 ppm in  
37 most terrestrial rocks (Capobianco and Watson, 1982; Rosenberg, 2008). The perceived  
38 banality of its distribution, coupled with the difficulty of achieving precise analyses at the  
39 required ppm level, explains why Ge has not been widely analysed in geochemical studies of  
40 igneous rocks. However, unlike Si, Ge is both a moderately siderophile and moderately  
41 volatile element, making it useful for testing models of accretion and core formation in the  
42 Earth, the Moon and other rocky planetary bodies (e.g. Schmitt et al., 1989; O'Neill 1991a, b;  
43 Walker et al., 1993; Hillgren et al., 1996; Jana and Walker, 1997a, 1997b, Capobianco et al.,  
44 1999; Holzheid et al., 2007; Righter et al., 2011; Siebert et al., 2011; Steenstra et al., 2016;  
45 Righter et al., 2017).

46 Evidence has accumulated that Ge occurs in the 2+ valence state at low  $f\text{O}_2$  in silicate melts.  
47 The evidence is based on the relationship between the distribution of Ge between Fe-rich  
48 metal and silicate melts ( $D_{\text{Ge}}^{\text{met/sil}}$ ) and  $f\text{O}_2$ ; this relationship is determined by the valence of  
49 Ge. The first report of  $\text{Ge}^{2+}$  by Schmitt et al. (1989) came as a surprise, because  $\text{Ge}^{2+}$  had not  
50 yet been observed in nature. It was not until 28 years later that  $\text{Ge}^{2+}$  was identified in  
51 sphalerite by X-ray absorption spectroscopy (XAS) (Bonnet et al. 2017), but this occurrence  
52 is with Ge bonded to sulfur, not oxygen. Synthetic compounds containing  $\text{Ge}^{2+}$ –O bonds are  
53 also rare and only three such compounds are listed in the ICSD database, namely  
54  $\text{GeCl}(\text{H}_2\text{PO}_2)$ ,  $\text{Na}[\text{Ge}_4(\text{PO}_4)_3]$ , and  $\text{Ge}_2(\text{H}_2\text{PO}_2)_6$  (Cempírek and Groat, 2013). Capobianco et  
55 al. (1999) were sceptical of the existence of  $\text{Ge}^{2+}$  in silicate melts, since their experiments  
56 indicated  $\text{Ge}^{4+}$  only. However, the  $f\text{O}_2$ s of their experiments were mostly higher than those of  
57 Schmitt et al. (1989) (see Figure 1). Kegler and Holzheid (2011) pointed out this discrepancy,  
58 and conducted a series of experiments that agreed well with the 2+ valence state obtained by  
59 Schmitt et al. (1989). In recent years, several further studies have investigated Ge valence  
60 below the IW buffer: a 2+ valence was reported by Righter et al. (2017) and Steenstra et al.  
61 (2017), and a nominal valence of 3+ (interpreted as a mixture of 2+ and 4+) was found by  
62 Siebert et al. (2011). The results of Vogel et al. (2018) were also consistent with a nominal  
63 3+ valence state, although they explained that the uncertainty was too large to constrain the  
64 valence robustly. Overall, most evidence suggests that  $\text{Ge}^{2+}$  occurs in silicate melts at  $f\text{O}_2$ s

65 below the IW buffer (Figure 1), at least to pressures up to 3 GPa and temperatures up to  
66 2200°C. These are the conditions pertinent to most rocky planetary bodies other than the  
67 Earth. Therefore, in these bodies, Ge would not be expected to be diadochic for Si but to have  
68 geochemical properties that are at present completely unknown.

69 Here we report an experimental study to constrain the  $fO_2$  range of the  $Ge^{4+}$ – $Ge^{2+}$  transition,  
70 using X-ray absorption near edge structure (XANES) spectroscopy. XANES is an element-  
71 specific technique, which is ideal for quantifying the oxidation state of trace elements (e.g.,  
72 Wong et al., 1984; Berry et al., 2003a; Berry and O'Neill, 2004). This technique has been  
73 used previously to distinguish  $Ge^0$ ,  $Ge^{2+}$ , and  $Ge^{4+}$  in sulfides, but never before for oxides  
74 (Pugsley et al., 2011; Cook et al., 2015; Belissont et al., 2016; Bonnet et al., 2017). We  
75 present XANES spectra of 19 glasses prepared at  $fO_2$ s ranging from IW -3 to IW +10. We  
76 also recorded the extended X-ray fine structure (EXAFS) spectrum of a  $Ge^{2+}$ –bearing sample  
77 to provide information about the structural incorporation of  $Ge^{2+}$  in melts and minerals.  
78 Finally, we report a first determination of the high-temperature geochemical behaviour of  
79  $Ge^{2+}$  in silicate systems from olivine–melt partitioning experiments. These experiments  
80 demonstrate that the geochemical behaviour of Ge was very different in the low  $fO_2$   
81 environments of most rocky planetary bodies from that found on Earth, which may account  
82 for the distribution of Ge in lunar rocks.

## 83 **2 Methods**

### 84 **2.1 Sample synthesis**

#### 85 *2.1.1 Starting materials*

86 Three CMAS compositions, named CMAS7G, AnDi and CMAS40 were used in this study.  
87 CMAS7G was used for melts equilibrated at atmospheric pressure because it is a good glass-  
88 former, and has a low liquidus temperature of 1129 °C (O'Neill and Eggins 2002). The AnDi  
89 composition was used for high-pressure experiments because it approximates a basaltic melt  
90 better. Both compositions were nominally free of Fe and other multivalent elements to avoid  
91 complications from electron exchange reactions (e.g.,  $Ge^{4+} + 2 Fe^{2+} = Ge^{2+} + 2 Fe^{3+}$ ), which  
92 may proceed rapidly enough to reset redox speciation on the timescale of quenching (e.g.,  
93 Berry et al., 2003). However, this problem may not have been entirely avoided in  
94 experiments with low levels of Ge due to some Fe contamination, typically at 300 to 400  
95 ppm, as discussed further in Section 4. For olivine–melt partitioning experiments, the MgO-

96 rich CMAS40 composition was used because this composition crystallises olivine on the  
97 liquidus at 1 GPa and 1500 °C – the same conditions at which the AnDi glasses were  
98 prepared. Here the reason for choosing an Fe-free composition was to avoid major-  
99 element compositional changes across the large range of  $fO_2$  encompassed by these  
100 experiments. Nominal starting compositions are given in the supplementary information  
101 (Table S1).

102 The glass compositions were prepared using reagent grade  $SiO_2$ ,  $Al_2O_3$ ,  $MgO$  and  $CaCO_3$ .  
103 These components were mixed under acetone and fired at 1050 °C to remove the carbonate.  
104 The CMAS40 composition was additionally doped with trace elements. Some samples,  
105 D2270 and C4444, were doped with  $GeO_2$  (0.46 wt%),  $Sc_2O_3$  (0.03 wt%),  $V_2O_3$  (0.12 wt%)  
106 and  $Y_2O_3$  (1.05 wt%), which were added as oxides. Other samples were doped with  $GeO_2$   
107 (0.27 wt%),  $Sc_2O_3$  (0.06 wt%),  $V_2O_3$  (0.18 wt%),  $Y_2O_3$  (0.50 wt%),  $TiO_2$  (0.52 wt%),  $HfO_2$   
108 (0.16 wt%),  $SrO$  (0.14 wt%),  $MnO_2$  (0.03 wt%),  $BaO$  (0.54 wt%),  $ZnO$  (0.02 wt%) and  $ZrO_2$   
109 (0.13 wt%).  $GeO_2$ ,  $TiO_2$ ,  $HfO_2$  and  $SrCO_3$  were added to the mixture as powders, but Y, Sc,  
110 V, Mn, Ba, Zn and Zr were added as AAS standard solutions, dissolved in 2% or 10%  $HNO_3$ ,  
111 except for Zn which was dissolved in 2% HCl. The powders and solutions were mixed  
112 together thoroughly in an agate mortar and then denitrified by firing as a pellet at 1050 °C  
113 overnight.

#### 114 2.1.2 Ambient-pressure experiments

115 Preparing silicate melts doped with Ge as a function of  $fO_2$  at atmospheric pressure is  
116 difficult because of the volatility of Ge, which increases with decreasing  $fO_2$  (e.g., Norris and  
117 Wood, 2017; Sossi et al., 2019). Our initial trials showed that near IW using the traditional  
118 approach of equilibrating melts in a gas-mixing furnace, as used in studies of non-volatile  
119 elements such as Fe and Cr (e.g., Berry et al., 2003a; Berry and O'Neill, 2004) resulted in the  
120 almost complete loss of Ge in a matter of a few minutes. To get around this problem, a new  
121 experimental design was implemented, inspired by O'Neill (2005) and Miller et al. (2019)  
122 (Figure 2).

123 Powdered samples of the CMAS7G composition were suspended on loops of Re ribbon with  
124 the aid of polyethylene oxide as glue. The mix was not doped with Ge; instead, Ge was added  
125 to the sample during the experiment by bathing the sample in Ge-containing vapour. To  
126 achieve this, the loop was hung in the top of a ~20 cm long silica tube, which was sealed at  
127 the bottom, but open at the top. Approximately 1 g of  $GeO_2$  powder was placed in the bottom

128 of the tube. The length of the tube was selected so that when the sample was at 1200 °C  
 129 (above the melting point of the CMAS7G composition) the bottom of the tube was at ~ 900  
 130 ±30 °C (cf. the melting point of GeO<sub>2</sub> is 1115 °C), which allowed the crystalline GeO<sub>2</sub> to  
 131 evaporate sufficiently slowly that it was not exhausted within the duration of the experiment.  
 132 The vapour, the dominant species in which is GeO (Barton and Heil, 1970), migrates up the  
 133 tube and flows past the sample. In some experiments, ceramic wool was placed in the middle  
 134 of the silica tube (and, in one experiment, D280116, at the top), to help slow the rate of GeO  
 135 vapour transfer. Since the tube was open at the top, the sample could equilibrate with the  $f_{O_2}$   
 136 in the furnace set by CO-CO<sub>2</sub> gas mixtures. The  $f_{O_2}$  was varied between IW +2 and IW -3.  
 137 Samples and their run conditions are listed in Table 1.

138 Table 1. Experimental conditions. The concentrations of Ge in the glasses were determined by LA-  
 139 ICPMS.

Sample	$\Delta IW$	Time (h)	Ge concentration (wt%)			$n^*$
			Overall	Edges	Interior	
<i>Glasses prepared at 1 atm and 1200 °C, composition CMAS7G, in a CO–CO<sub>2</sub> gas mix</i>						
D210116	+2.0	6.8	1.22 (31)	1.03 (29)	1.46 (7)	7, 4
D171215	+1.0	8	0.71 (11)	0.66 (11)	0.75 (10)	5, 5
D191215	+0.5	8	0.34 (5)	–	–	5
D301115	0.0	14	0.28 (10)	0.21 (9)	0.34 (3)	6, 5
D181215	-0.5	7.5	0.22 (2)	0.22 (1)	0.21 (2)	5, 5
D151215	-1.0	7.5	0.15 (2)	0.14 (2)	0.16 (2)	5, 5
D140416	-1.0	5	0.07 (4)	0.03 (1)	0.11 (1)	3, 3
D250116	-1.5	7.5	0.053 (6)	–	–	3
D160416	-1.5	5	0.041 (8)	0.035 (8)	0.047 (2)	3, 3
D280116	-1.75	6	0.041 (9)	0.045 (5)	0.038 (11)	3, 3
D170416	-2.5	4.2	0.050 (9)	0.043 (7)	0.058 (1)	3, 3
D120416	-3.0	4.8	0.065 (8)	0.058 (4)	0.071 (5)	3, 3
<i>Glasses prepared at 1 atm and 1300 °C, composition CMAS7G, in air</i>						
E021213B	+10.1	4	2.08 (3)			3
B1-080316	+10.1	0.25	0.29 (1)			6
E041113**	+10.1	4	0.21 (1)			3
E021213A	+10.1	4	0.03 (1)			4
<i>Glasses prepared at 1 GPa and 1500 °C, composition AnDi</i>						
C5201	-1.3 (2)	24	0.18 (2)			5
C5204	-0.9 (2)	24	0.66 (1)			6
C5234	0.3 (2)	10.5	3.3 (2)			5
C5206	0.4 (2)	24	4.04 (3)			6
<i>Partitioning experiments conducted at 1 GPa and 1500 °C, composition CMAS40</i>						
D2270	-9.5 (2)	< 24 <sup>†</sup>				
D2357	-7.2 (3)	24				
D2368-i	-0.7 (2)	48				
D2368-ii	-0.7 (2)	48				
C4444	+8.6	24				
D2413	+8.6	24				

140 \* $n$  = number of analyses (edge, interior). Two samples, D191215 and D250116, were so small (<2  
 141 mm) that edge and interior analyses were not collected. Numbers in parentheses are one standard  
 142 deviation on the last digit. \*\*E041113A was used for EXAFS only. <sup>†</sup>Sample D2270 quenched before  
 143 24 h due to a failure with the apparatus. Note that the values of  $\Delta IW$  given for the glasses prepared at  
 144 1 atm are nominal values set by the mixture of CO–CO<sub>2</sub> gases. Values given for other samples were  
 145 calculated from the Co–CoO, Ni–NiO, and Ru–RuO<sub>2</sub> equilibria as described in Section 3.2.

146

147 Quenching the sample to glass in this setup was not entirely straightforward. In all  
148 experiments, the tube was dropped into a bucket of water by releasing the mechanism that  
149 held the tube in place (see O'Neill and Berry, 2006). To facilitate rapid quenching, slits were  
150 cut in the sides of the tube in some experiments, which encouraged the tube to break when it  
151 hit the bottom of the bucket, thereby enabling water to quickly come into contact with the  
152 sample.

### 153 2.1.3 High-pressure experiments

154 Glasses and olivine–melt partitioning experiments were equilibrated at 1500 °C and 1 GPa  
155 using a 200 T end-loaded Boyd-England type piston cylinder apparatus. Samples are listed in  
156 Table 1. The samples were contained in graphite capsules with a layer of Ge and either Co or  
157 Ni metal powders (1:1 ratio by weight) at the bottom. The layer of metals served as a source  
158 of Ge and enabled the calculation of  $fO_2$  retrospectively from the Ni or Co contents of the  
159 resulting melts and Ge-Ni or Ge-Co alloys. The metal mixtures comprised 10–25 wt% of the  
160 sample. In some capsules a small amount of Si metal (1–7 wt% of the sample) was also  
161 added to further lower the  $fO_2$ . Two of the partitioning experiments were carried out using Pt  
162 capsules and 20 wt% Ru-RuO<sub>2</sub> oxygen buffer (80% RuO<sub>2</sub>, 20% Ru), for which  $\log fO_2 = IW$   
163 +8.6 at 1500 °C (O'Neill and Nell, 1997).

164 The capsules were placed in an assembly comprising concentric layers of MgO, graphite  
165 (heater), Pyrex, and NaCl. This assembly was wrapped in Teflon foil and inserted into a  
166 pressure vessel with a bore size of either a 1/2" (C4444 and D2413) or 5/8" (all other  
167 experiments). Temperature was monitored using a Type B thermocouple, sheathed in mullite  
168 with a 5-mm alumina tip. The samples were equilibrated for 10–48 h (see Table 1), at 1500  
169 °C and 1 GPa, before quenching by cutting power to the heater. In one experiment (D2368)  
170 two capsules were run together, with suffixes 'i' and 'ii' arbitrarily assigned.

### 171 2.1.4 Standards for XAS

172 Ideally, compounds containing Ge in known valence states and coordination environments  
173 ('standards') are required for comparison with the samples prepared. Five Ge<sup>4+</sup> standards  
174 were prepared: Ge<sup>4+</sup>O<sub>2</sub> in the quartz form (q-GeO<sub>2</sub>), and four Ge-doped glasses quenched  
175 from melts that were equilibrated in air. The q-GeO<sub>2</sub> sample was made by firing GeO<sub>2</sub>  
176 powder at 1060 °C for 24 h in air, to ensure that the powder did not contain any of the rutile

177 form of GeO<sub>2</sub> (Laubengayer and Morton, 1932). The glass samples (listed in Table 1) were  
178 made using the CMAS7G composition, doped with different amounts of Ge (~300 ppm,  
179 ~2100 ppm and ~2 wt%). These mixes were loaded into Pt capsules that were welded shut at  
180 one end, but only crimped at the other. The 300-ppm (E021213A) and 2-wt% (E021213B)  
181 samples were heated in the furnace together at 1300 °C, and the 2100-ppm sample (E041113)  
182 was heated in a separate experiment at the same temperature. All samples were heated for 4 h  
183 in air before quenching in water. An additional sample (B1-080316) was prepared by heating  
184 CMAS7G, doped with ~2900 ppm Ge, in an alumina crucible at 1300 °C for 15 min. in air  
185 before quenching in water.

186 For Ge<sup>0</sup> standards, we used two samples of amorphous silica that had been implanted with  
187 Ge<sup>0</sup>, described in Ridgway et al. (2004). One sample was prepared by implanting Ge atoms  
188 into amorphous silica to give a concentration of  $3 \times 10^{17}$  atoms cm<sup>-2</sup> (Ge<sup>(imp)</sup>). A second  
189 sample was prepared by annealing the Ge-implanted silica at 1100 °C, which led to the  
190 formation of crystalline Ge nanoparticles 5–10 nm in size (Ge<sup>(ann)</sup>). These standards were  
191 used rather than Ge metal, because they should better represent how Ge<sup>0</sup> might be present in  
192 the silicate melt: either as dissolved Ge<sup>0</sup> atoms or as Ge metal ‘nuggets’.

193 No Ge<sup>2+</sup> standards were available. Ge<sup>2+</sup> does not readily form oxides, and compounds  
194 containing Ge<sup>2+</sup> bonded to S, Se or I would not be good standards because the XANES  
195 spectra vary greatly with the ligand (Pugsley et al., 2011).

## 196 2.2 Sample characterisation

197 Samples were mounted in epoxy, sectioned and polished. The glass samples were examined  
198 by optical microscopy (100× objective with a numerical aperture = 1.4, ∞/0, and Type A  
199 immersion oil, n = 1.515).

200 Major element concentrations of 1-atm glasses and the partitioning experiments were  
201 determined using a Hitachi S4300 SE/N Field Emission Scanning Electron Microscope (FE-  
202 SEM) fitted with an Oxford X-Max EDS detector. The operating conditions were 15 kV  
203 accelerating voltage, 0.600 nA beam current, and a working distance of 25 mm. Standards  
204 were MgO for Mg, albite for Al, sanidine for Si, diopside for Ca, TiO<sub>2</sub> for Ti, Co metal for  
205 Co, and La<sub>8</sub>Sr<sub>2</sub>Ge<sub>6</sub>O<sub>26</sub> for Ge.

206 Major element concentrations of high-pressure glasses and metal alloys were determined by  
207 electron probe microanalysis (EPMA) using a CAMECA SX100, operating at 20 kV. Beam  
208 currents used were 10 nA for the silicate glasses and 20 nA for the metal alloys. A  
209 defocussed beam was used, with a diameter of 20  $\mu\text{m}$  for the silicate glasses, and between 10  
210 and 50  $\mu\text{m}$  for the metal alloys. For analyses of silicate glasses, calibration standards were  
211 quartz for Si, corundum for Al, augite for Ca, San Carlos olivine for Fe, and the  
212 corresponding pure metals for Ge, Ni, Co, and Y. Magnesium, Al and Si were analysed at the  
213 K- $\alpha$  lines using a TAP crystal, Ca and Y (K- $\alpha$  and L- $\alpha$  lines respectively) using a PET  
214 crystal, and Ge, Ni, Co and Fe using two LLIF crystals (K- $\alpha$  lines). For alloy analyses, the  
215 calibration standards were pure metals of Ge, Si, Ni and Co. Germanium and Si were  
216 measured using a TAP crystal (L- $\alpha$  and K- $\alpha$  lines respectively) and Ni and Co using a LLIF  
217 crystal (K- $\alpha$  lines).

218 Trace element concentrations were determined by Laser-Ablation Inductively Coupled  
219 Plasma Mass Spectrometry (LA-ICPMS) using an excimer laser with a wavelength of 193  
220 nm and a pulse rate of 5 Hz, coupled to an Agilent 7700 ICP-MS with He+Ar as the carrier  
221 gas. Samples were ablated for  $\sim 40$  s, with  $\sim 20$  s of background measured for each spot. The  
222 external standard was NIST 610 glass and Si was used as the internal standard. The spot size  
223 was between 22 and 47  $\mu\text{m}$ . An in-house Excel spread sheet was used to reduce the data.

## 224 2.3 X-ray absorption spectroscopy

225 Germanium K-edge X-ray absorption near edge structure (XANES) spectra and extended X-  
226 ray absorption fine structure (EXAFS) spectra were recorded at the X-ray Absorption  
227 Spectroscopy (XAS) beamline of the Australian Synchrotron (operating at 200 mA in Top-  
228 Up mode of operation). The XAS beamline utilizes a 1.6T wiggler, Rh coated Si collimating  
229 mirror, cryo-cooled Si(111) monochromator and Rh coated torodial refocusing mirror. The  
230 X-ray beam spot at the sample was set at ca.  $0.5 \times 0.5$  mm. The incident X-rays had an  
231 energy resolution  $\Delta E/E$  of  $\sim 1/7000$ . The energy was calibrated by defining the first  
232 derivative peak in the spectrum of Au foil recorded in transmission mode to be at 11919.7  
233 eV. The energy reproducibility over the experiment was better than 0.05 eV.

234 XAS spectra were recorded in fluorescence mode using a 100-element Ge detector, with the  
235 polished surface of the sample positioned at  $45^\circ$  to the incident beam and the detector at  $90^\circ$   
236 to the incident beam. For XANES spectra, the distance between the detector and the sample  
237 was varied according to the Ge content of the sample, in order to maintain a nearly constant

238 count rate at the white line, which was within the linear range of the signal processing  
239 electronics. XANES spectra were recorded at room temperature using a 8 eV step size for the  
240 pre-edge region (10903–11083 eV), a 0.25 eV step size for the near-edge region (11083–  
241 11153 eV) and a 0.1 Å<sup>-1</sup> step size for the post-edge (11153–11489 eV, k=10) regions. The  
242 EXAFS were recorded at 10 K using intervals of 0.035 Å<sup>-1</sup> for the EXAFS region regions  
243 (11153-12084 eV, k=16 for standards and 11153–11855 eV, k=14 for the Ge<sup>2+</sup> spectrum).  
244 The spectrum of Ge<sup>(imp)</sup> was recorded in a previous experiment conducted by the authors at  
245 the same beamline, using the same setup but with minor differences in count rates and step  
246 sizes, detailed in the supplementary information (section S2).

247 To determine whether the X-ray beam induced changes in Ge speciation, two spectra were  
248 recorded consecutively at the same spot on samples prepared at IW -3 and IW -2.5.  
249 Monitoring fast changes in intensity at a single energy was not possible because the detector  
250 had a slow response time to significant changes in count rate (e.g., on opening the shutter).

251 For each spectrum, the signals from all detector elements were averaged and divided by the  
252 incident photon flux. Normalisation and background subtraction of XANES spectra were  
253 performed using the program ATHENA, and EXAFS spectra were fit using ARTEMIS after  
254 merging and de-glitching in ATHENA (Ravel and Newville, 2005)

## 255 **3 Results**

### 256 **3.1 Experimental products**

257 The samples prepared at ambient pressure were glasses containing few quench crystals and  
258 many metallic micronuggets. LA-ICPMS ablation profiles for Re show large spikes  
259 indicating the presence of micronuggets, similar to those observed by Ertel et al. (2001); no  
260 spikes were observed for Ge, indicating that the observed micronuggets were derived from  
261 the Re wire used to suspend the sample. Major-element compositions of several 1-atm  
262 glasses are given in the supplementary information (Table S2). Germanium concentrations,  
263 listed in Table 1, differ greatly between samples. In general, more reduced samples contain  
264 less Ge, probably due to its greater volatility at lower *f*O<sub>2</sub>. Germanium concentrations were  
265 also quite heterogeneous and were lower near the edges of a sample than in the middle.

266 The high-pressure samples contained a large sphere of metal alloy (>100 μm) at one end of  
267 the capsule, often accompanied by several smaller blobs (~5–30 μm), as well as clusters of

268 metal nuggets (<5 μm) near the edges of the capsule, but these were easily avoided during  
 269 analysis of the glass. The compositions of the 5–30 μm-sized blobs were typically within 1  
 270 mol% of the larger mass, and all analyses were averaged for calculating  $fO_2$  (Table 2). The  
 271 Ge concentrations of the silicate glasses in the high-pressure samples are given in Table 1,  
 272 and major element compositions of the silicate glasses are given in the supplementary  
 273 information (Table S3).

274 Table 2. Compositions (mol%) of metal alloys in high-pressure experiments, CoO or NiO  
 275 concentration (mol%) in the melt, and calculated  $fO_2$  relative to IW.

	Ge in alloy	Co or Ni* in alloy	Si in alloy	CoO or NiO* in melt	$\Delta IW$
<i>Glass experiments</i>					
C5201*	36.6 (9)	63.4 (8) *	n.d.	0.025 (1) *	-1.3 (2)
C5204	41.1 (2)	58.7 (2)	0.11 (2)	0.41 (2)	-0.9 (2)
C5206	38.2 (2)	61.7 (3)	0.10 (1)	2.05 (1)	0.4 (2)
C5234	38.5 (3)	61.3 (3)	0.10 (2)	1.86 (5)	0.3 (2)
<i>Partitioning experiments</i>					
D2270	30.2 (17)	41.1 (21)	28.8 (24)	$7 (1) \times 10^{-6}$	-9.5 (2)
D2357	36.0 (15)	51.2 (5)	12.7 (13)	$2.0 (5) \times 10^{-5}$	-7.2 (3)
D2368-i	44.1 (6)	55.7 (6)	0.12 (4)	0.44 (1)	-0.7 (2)
D2368-ii	45.2 (4)	54.7 (5)	0.15 (4)	0.39 (2)	-0.7 (2)

276 \*C5201 contains Ni, all other samples contain Co. n.d. = not detected.  
 277

### 278 3.2 $fO_2$ of high-pressure samples

279 The  $fO_2$  of the high-pressure samples was calculated from the Co and Ni contents of the  
 280 coexisting alloys and melts (Kegler and Holzheid, 2011), using:

$$281 \quad \Delta[M-MO] = 2 \cdot \log \frac{X_{MO} \cdot \gamma_{MO}}{X_M \cdot \gamma_M} \quad \text{Equation 1}$$

282 where M is the metal used in the experiment (Co or Ni),  $\Delta[M-MO]$  is the  $\log fO_2$  relative to  
 283 the buffer (Co–CoO or Ni–NiO),  $X_M$  and  $\gamma_M$  are the mole fraction and activity coefficient,  
 284 respectively, of the metal in the alloy, and  $X_{MO}$  and  $\gamma_{MO}$  are the mole fraction and activity  
 285 coefficient, respectively, of the metal oxide in the silicate melt.

286 The activity coefficients of CoO and NiO in silicate melts are  $1.51 \pm 0.28$  and  $2.70 \pm 0.52$   
 287 respectively (Holzheid et al. 1997). Activity coefficients of Ni or Co in the alloy were  
 288 obtained from thermodynamic studies of the binary Ge–Co or Ge–Ni liquids (Nash and  
 289 Nash, 1987; Ishida and Nishizawa, 1991). These activity coefficients were interpolated to  
 290 estimate the activity at the concentration measured in our samples. Some of the alloys in the  
 291 experiments also contain Si (see Table 2), which we assume has a negligible effect on the  
 292 activity coefficients. This assumption is probably reasonable for most of the samples, in

293 which the Si contents were <0.2 mol%. However, in the two most reduced partitioning  
294 experiments (D2270 and D2357), the alloys contained 13 and 29 mol% Si respectively, so the  
295 results for these samples should be treated with caution. The final step in the calculation is to  
296 convert the values of  $\Delta[\text{Co-CoO}]$  or  $\Delta[\text{Ni-NiO}]$  to  $\Delta\text{IW}$  (O'Neill and Pownceby, 1993). The  
297 effect of pressure on the  $f\text{O}_2$  of all buffers is similar at 1 GPa (Frost, 1991), and so the  
298 pressure effect was ignored in the conversion. The calculated  $\Delta\text{IW}$  values are given in Table  
299 2.

### 300 3.3 X-ray absorption spectroscopy

#### 301 3.3.1 XANES

302  
303 Germanium K-edge XANES spectra of all samples and standards are shown in Figure 3. The  
304 spectra of the  $\text{Ge}^0$  standards are expected to have lower edge energy than those of the  $\text{Ge}^{4+}$   
305 standards, and this is observed (Figure 3). The spectra of the glasses equilibrated at high  $f\text{O}_2$   
306 are very similar to the spectrum of q- $\text{GeO}_2$ , but with decreasing  $f\text{O}_2$  the spectra of the glasses  
307 develop a shoulder at 11108 eV. This shoulder grows in intensity and becomes a peak in the  
308 spectra of samples equilibrated at low  $f\text{O}_2$ , although this trend is not completely systematic  
309 (as discussed further in Section 4.2). The shoulder at 11108 eV cannot be attributed to the  
310 presence of  $\text{Ge}^0$  in the samples because the absorption edge of  $\text{Ge}^0$  is at lower energy and the  
311 spectra have a very different shape (note that the differences between the two  $\text{Ge}^0$  spectra  
312 result from the differences in Ge environments between implanted and annealed samples; see  
313 Ridgway et al. 2004). The absorption edge of  $\text{Ge}^0$  can be seen as the first peak in the  
314 derivative spectrum (Figure 3B), and there is no component of  $\text{Ge}^0$  observed in the derivative  
315 spectra of any of the glasses. Therefore, we attribute the peak at 11108 eV to  $\text{Ge}^{2+}$ . The edge  
316 energies of  $\text{Ge}^0$ ,  $\text{Ge}^{2+}$  and  $\text{Ge}^{4+}$  increase systematically (see Figure S1). The spectra attributed  
317 to  $\text{Ge}^{2+}$  appeared to be stable under the X-ray beam: spectra recorded consecutively at the  
318 same spot were very similar (each spectrum took about 30 min. to acquire). The only change  
319 was a slight (~2%) decrease in the intensity of the white line in the second spectrum from  
320 each sample.

321 We tested for effects of concentration by recording spectra for samples containing ~300 ppm,  
322 ~2900 ppm and ~2 wt% Ge (Figure 4). The spectrum of the sample with the lowest  
323 concentration of Ge exhibits a small shoulder on the low-energy side of the absorption edge,

324 at the same energy as the peak attributed to Ge<sup>2+</sup>. The spectra of the 2900-ppm and 2-wt%  
325 samples are almost identical and do not exhibit this shoulder.

326 Several approaches were taken to quantify the relative changes between each spectrum.  
327 These approaches were based on either quantifying spectral features or linear combination  
328 fitting of end-members. We quantified six spectral features: (1) the intensity of the ‘Ge<sup>2+</sup>  
329 peak’ at 11108 eV, (2) the intensity of the ‘Ge<sup>4+</sup> peak’ at 11112 eV (3) the area under the  
330 ‘Ge<sup>2+</sup> peak’ between 11105 and 11110 eV (4) the area under the ‘Ge<sup>4+</sup> peak’ between 11110  
331 and 11115 eV, (5) the area under the ‘Ge<sup>2+</sup> peak’ in the derivative spectrum between 11102  
332 and 11108 eV, and (6) the area under the ‘Ge<sup>4+</sup> peak’ in the derivative spectrum between  
333 11108 and 11112 eV. The results of the latter (6) are plotted against ΔIW in Figure 5A as an  
334 example of the ‘spectral features’ approach, but all six of these methods gave similar results  
335 (see Table S4 and Figure S2).

336 For the linear combination fitting approach, six spectra were considered suitable as ‘end-  
337 members’. These spectra are D120416, D170416 and D280116 for the Ge<sup>2+</sup> end-member, and  
338 D210116, B1-080316, and E021213B for the Ge<sup>4+</sup> end-member. With three choices for each  
339 end-member, nine sets of linear combination fits were produced. Each spectrum was fit to the  
340 equation:

$$341 \quad y = a \cdot \text{Ge}^{4+} \text{ end-member} + (1 - a) \cdot \text{Ge}^{2+} \text{ end-member} \quad \text{Equation 2}$$

342 where  $a$  is the fit parameter, representing the proportion of the Ge<sup>4+</sup> end-member in the  
343 spectrum, and  $y$  is the predicted curve. The difference between each unknown spectrum and  
344 the predicted spectrum,  $y$ , was minimized by adjusting the fit parameter,  $a$ . The fit parameter  
345 based on one combination of end-members is plotted against ΔIW in Figure 5B, however all  
346 combinations of end-members gave similar results (Table S5, Figure S3 and S4).

347 There could be several sources of error on the data points shown in Figure 5. These include  
348 noise in the spectra, energy drifts, and sample preparation techniques. The spectra have only  
349 low levels of noise ( $\pm 0.02$  units of normalised intensity), and a Monte-Carlo approach  
350 showed that this level of noise would produce standard deviations smaller than the size of the  
351 symbols in Figure 5A. The standard errors on the linear combination fit parameters are also  
352 smaller than the size of the symbols in Figure 5B. The potential for errors due to energy drift  
353 at the beamline can be assessed using two replicate spectra that were acquired of D120416.  
354 The spectral features (intensities and areas) calculated from these two replicate spectra differ

355 by 6% at most, also smaller than the size of the symbols. Therefore, the deviation of the  
 356 results from a sigmoid cannot be attributed to errors arising from noise or energy drift in the  
 357 spectra, and may instead relate to the sample synthesis procedures, as described in Section  
 358 4.2.

359 The oxidation state of a redox-variable element such as Ge in a glass can be described by  
 360 (Berry and O'Neill 2004):

$$361 \frac{\text{Ge}^{4+}}{\Sigma\text{Ge}} = \frac{1}{1+10^{-\left(\frac{n}{4}\log f\text{O}_2 + \log K'\right)}} \quad (3)$$

362 This equation describes oxidation state (where  $\Sigma\text{Ge} = \text{Ge}^{4+} + \text{Ge}^{2+}$ ) as a sigmoidal function of  
 363  $\log f\text{O}_2$  relative to IW, where the slope is determined by the number of electrons involved in  
 364 the reaction ( $n$ ), and the position in  $\log f\text{O}_2$  space is defined by the parameter  $\log K'$ . In order  
 365 to rewrite Eq. (3) in terms of  $\Delta\text{IW}$ , we define:

$$366 \log K'' = \log K' + \frac{n}{4}\log f\text{O}_2^{\text{IW}} \quad (4)$$

367 where  $\log f\text{O}_2^{\text{IW}}$  is the  $\log f\text{O}_2$  at the IW buffer. Setting  $n = 2$  for the two-electron reaction, we  
 368 can rewrite Eq. (3) as:

$$369 \frac{\text{Ge}^{4+}}{\Sigma\text{Ge}} = \frac{1}{1+10^{-\left(\frac{1}{2}\Delta\text{IW} + \log K''\right)}} \quad (5)$$

370 In order to fit the spectral features to this function, we follow the approach of Berry and  
 371 O'Neill (2004) and Burnham et al. (2015), by recasting Eq. (5) in terms of the variation of a  
 372 spectral feature with  $\log f\text{O}_2$ . This involves the addition of parameters  $a$  and  $c$  that define the  
 373 value and baseline of the feature:

$$374 \text{Feature} = \frac{a}{1+10^{-\left(\frac{1}{2}\Delta\text{IW} + \log K''\right)}} + c \quad (6)$$

375 For each spectral feature that was quantified, the data were fit to Equation 4 and the fit  
 376 parameters are given in Table 3. The 1-atm and high-pressure data were fit separately, shown  
 377 as the black and red curves in Figure 5A. Two data points were omitted from the fit – sample  
 378 E021213A, which exhibits an anomalous shoulder at 11108 eV, and sample E041113, for  
 379 which the spectrum was recorded in EXAFS mode with a count rate three times higher than  
 380 the XANES spectra. The high-pressure data do not span a wide enough  $f\text{O}_2$  range to robustly

381 fit parameters  $a$  and  $c$ , so these parameters were fixed to be the same as found for the low-  
382 pressure data, while  $\log K''$  was allowed to vary. Taking the different fitting methods into  
383 account, we find that  $\log K'' = 0.15(28)$  for the low-pressure data and  $0.52(63)$  for the high-  
384 pressure data (Table 3).

385

386 Table 3. Fit parameters resulting from fits of Equation 6 or Equation 5 to the spectral features or linear  
 387 combination fit results, respectively. CI is  $\pm 95\%$  confidence interval on the parameter. MSE is mean  
 388 square error, a measure of the goodness-of-fit.

	Low-pressure				High-pressure					
	<i>a</i>	CI	<i>c</i>	CI	$\log K''$	CI	MSE	$\log K''$	CI	MSE
<i>Spectral features</i>										
Ge <sup>2+</sup> peak height	-2.14	0.32	2.66	0.29	0.12	0.27	0.03	0.55	0.53	0.11
Ge <sup>4+</sup> peak height	1.01	0.17	1.31	0.16	0.19	0.30	0.01	0.48	0.74	0.05
Ge <sup>2+</sup> peak area	-7.25	1.15	9.62	1.00	0.11	0.28	0.41	0.53	0.52	1.17
Ge <sup>4+</sup> peak area	3.22	0.56	6.37	0.51	0.19	0.30	0.09	0.50	0.87	0.67
Ge <sup>2+</sup> deriv. area	-2.10	0.32	2.50	0.28	0.12	0.27	0.03	0.55	0.53	0.10
Ge <sup>4+</sup> deriv. area	3.14	0.47	-1.33	0.42	0.15	0.27	0.07	0.53	0.61	0.31
Averages					<b>0.15</b>	<b>0.28</b>		<b>0.52</b>	<b>0.63</b>	
					logK'' 1 $\sigma$ = 0.04			logK'' 1 $\sigma$ = 0.03		
<i>LCF of end-members</i>										
B1-080316 & D120416					0.00	0.16	0.010	0.46	0.66	0.037
B1-080316 & D170416					0.03	0.15	0.009	0.48	0.64	0.036
B1-080316 & D280116					0.02	0.16	0.009	0.46	0.65	0.037
D210116 & D120416					0.04	0.17	0.011	0.49	0.65	0.037
D210116 & D170416					0.07	0.16	0.010	0.51	0.64	0.035
D210116 & D280116					0.05	0.17	0.011	0.50	0.65	0.036
E021213B & D120416					-0.02	0.16	0.009	0.42	0.62	0.034
E021213B & D170416					0.01	0.15	0.008	0.44	0.61	0.033
E021213B & D280116					-0.01	0.16	0.009	0.43	0.62	0.034
Averages					<b>0.02</b>	<b>0.16</b>		<b>0.46</b>	<b>0.64</b>	
					logK'' 1 $\sigma$ = 0.03			logK'' 1 $\sigma$ = 0.03		

389

390 A sigmoidal function was also fit to the results from linear combination fitting using  
 391 Equation 5 (see Figure 5B and Table 3). The  $\log K''$  values obtained compare well with the  
 392 results from the spectral features. However, linear combination fitting assumes that the pure  
 393 Ge<sup>2+</sup> end-member has been obtained. The approach based on spectral features does not  
 394 assume a pure Ge<sup>2+</sup> end-member, and predicts a small component of Ge<sup>4+</sup> in the most  
 395 reducing samples.

### 396 3.3.2 EXAFS

397 The EXAFS spectra of q-GeO<sub>2</sub>, D120416 (predominantly Ge<sup>2+</sup>), and E041113 (Ge<sup>4+</sup>) are  
 398 shown in Figure 6. The EXAFS are highly damped in the Ge<sup>2+</sup> spectrum, and the Fourier  
 399 transform indicates that the Ge–O bond length is longer than for Ge<sup>4+</sup>. Fits to the spectra are  
 400 shown as red curves in Figure 6.

401 Four paths were used to fit q-GeO<sub>2</sub>: single scattering from first-shell O, single scattering from  
 402 second-shell Ge, single scattering from third-shell O and double scattering from first-shell O  
 403 and second-shell Ge. The data were fit in R space, over the range 1.0–3.2 Å, and a k-range of  
 404 3–14 Å<sup>-1</sup>. These four paths contributed most to the spectrum and adding more paths did not  
 405 improve the fit. The fitted GeO<sub>2</sub> path lengths were all within ± 1.5% of the reference values  
 406 (see Table 4).

407 Table 4. EXAFS fit parameters for spectra of q-Ge<sup>4+</sup>O<sub>2</sub>, a Ge<sup>4+</sup>-bearing glass (E041113), and Ge<sup>2+</sup>-  
 408 bearing glass (D120416).

Path	q-GeO <sub>2</sub> (Ge <sup>4+</sup> )				E041113 (Ge <sup>4+</sup> )	D120416 (Ge <sup>2+</sup> )
	[Ge]–O.1	[Ge]– Ge.1	[Ge]–O.2– Ge.1	[Ge]–O.3	[Ge]–O.1	[Ge]–O.1
N	4	4	8	4	4	3.4 (10)
S <sub>0</sub> <sup>2</sup>	0.95 (5)	0.95	0.95	0.95	0.87 (5)	0.87
σ <sup>2</sup> (Å <sup>2</sup> )	0.0034 (7)	0.0021 (5)	0.010 (10)	-0.001 (1)*	0.0017 (6)	0.008 (5)
E <sub>0</sub> (eV)	5.9 (7)	5.9	5.9	5.9	6.0 (9)	9 (4)
Δr (Å)	0.019 (5)	0.013 (7)	0.029 (68)	-0.049 (17)	0.011 (5)	0.15 (3)
Reference path length (Å) *	1.739	3.153	3.316	3.406	1.739	1.739
Path length in sample (Å) **	1.758 (5)	3.166 (7)	3.345 (68)	3.357 (17)	1.750 (5)	1.89 (3)

409 N is the degeneracy (for first-shell oxygens, this equals the coordination number), S<sub>0</sub><sup>2</sup> is the amplitude  
 410 reduction factor, σ<sup>2</sup> is the mean square relative displacement, E<sub>0</sub> is the difference in reference energy  
 411 compared to the standard, Δr is the change in half-path length compared to the 'reference path  
 412 length'. \*The 'reference path length' was calculated from the lattice parameters of GeO<sub>2</sub> (Smith and  
 413 Isaacs, 1964). \*\* The 'path length in sample' is calculated by adding Δr to the 'reference path length'.  
 414 Paths are from the central atom [Ge] to one or more surrounding atoms. For example, [Ge]–O.1 refers  
 415 to scattering from first-shell oxygen atoms. Errors on the last digit are provided in parentheses; values  
 416 without errors quoted were constrained in the fit. \*The negative value of σ<sup>2</sup> obtained for the [Ge]–O.3  
 417 path of q-GeO<sub>2</sub> does not make physical sense, but it is within error of zero.

418

419 To fit the spectra of the glass samples, only one path was used – single scattering from first-  
 420 shell O. The spectra of the glasses were fit in R-space over the range 1.0–2.0 Å. The Ge<sup>4+</sup>  
 421 glass was fit over a k-range 3–14 Å<sup>-1</sup>, whereas the range was only 3–10 Å<sup>-1</sup> for the Ge<sup>2+</sup>  
 422 sample due to the damped data. For the Ge<sup>4+</sup>-bearing glass the coordination number (N) was  
 423 fixed at 4 and the other parameters were allowed to vary in the fit. For the Ge<sup>2+</sup>-bearing  
 424 glass, three fits were performed. In the fit shown in Figure 6, and listed in Table 4, the  
 425 coordination number was allowed to vary, but S<sub>0</sub><sup>2</sup> was fixed at the value obtained for the  
 426 Ge<sup>4+</sup>-bearing glass. The Ge-O bond lengths were equal within error if S<sub>0</sub><sup>2</sup> was allowed to  
 427 vary with N fixed at 4, or if both N and S<sub>0</sub><sup>2</sup> were fixed. The Ge<sup>4+</sup>-O bond length in glass

428 obtained by EXAFS is 1.750(5) Å, which is only 0.6% longer than the reference value of  
429 Ge<sup>4+</sup>–O in the quartz form of GeO<sub>2</sub>. In contrast, the Ge<sup>2+</sup>–O bond length is found to be  
430 1.89(3) Å; this is 9% longer than the reference value.

431 The Ge<sup>2+</sup>–O bond length of 1.89(3) Å obtained from the EXAFS is in good agreement with  
432 bond lengths in the only structurally characterized oxide compounds with Ge<sup>2+</sup> coordinated to  
433 O<sup>2-</sup>, namely GeCl(H<sub>2</sub>PO<sub>2</sub>), Ge<sub>2</sub>(H<sub>2</sub>PO<sub>2</sub>)<sub>6</sub> and NaGe<sub>4</sub>(PO<sub>4</sub>)<sub>3</sub>. The bond lengths in the latter  
434 crystal, which has two distinct Ge<sup>2+</sup> sites, where in both cases Ge<sup>2+</sup> is bonded only to oxygen,  
435 average 1.91(1) Å, range 1.86 to 1.93 Å (Lee and Weng 2008). According to Cempírek and  
436 Groat (2013), Ge<sup>2+</sup> typically occurs in compounds with oxides or halides in triangular  
437 pyramidal coordination, that is, a distorted tetrahedral coordination, in which a lone pair of  
438 electrons is directed opposite to the triangle of anions. This stereochemistry implies a  
439 considerable degree of covalent bonding between the lone pair and its nearest neighbour  
440 anion. The coordination number obtained by EXAFS fitting is 3.4 ± 1.0, which is consistent  
441 with this conclusion.

## 442 3.4 Partitioning experiments

### 443 3.4.1 *Experimental olivine-melt partitioning results*

444 A typical run product from a partitioning experiment is shown in Figure 7. The  
445 concentrations of major and trace elements in olivine and melt, and the partition coefficients,  
446 are given in Table 5. The *f*O<sub>2</sub>s of these partitioning experiments were calculated using the  
447 Co–CoO equilibrium in Section 3.2. However, it is also possible to calculate the *f*O<sub>2</sub> from the  
448 partitioning of V between olivine and silicate melt using equation 5 from Mallmann and  
449 O'Neill (2013). This equation is only calibrated for an *f*O<sub>2</sub> range of IW -0.6 to +7.4 and so is  
450 only applicable for samples D2368-i and -ii, for which ΔIW = -0.7(2) based on the Co–CoO  
451 equilibrium. Using the V partitioning approach gives ΔIW = -0.42(6), and -0.47(10) for  
452 D2368-i and -ii respectively. The *f*O<sub>2</sub>s determined by both methods thus agree within error.

453 Table 5. Major and trace element composition of samples determined by EDS and LA-ICPMS, and partition coefficients ( $D^{ol/melt}$ ).

	D2270			D2357			D2368-i		
	Olivine	Melt	$D^{ol/melt}$	Olivine	Melt	$D^{ol/melt}$	Olivine	Melt	$D^{ol/melt}$
Major elements by EDS (wt%)									
<i>n</i>	4	9	—	5	6	—	3	4	—
MgO	57.7 (3)	27 (2)	2.2 (2)	57.5 (3)	29.9 (2)	1.93 (2)	56.5 (3)	27.8 (5)	2.03 (4)
Al <sub>2</sub> O <sub>3</sub>	0.16 (1)	10.8 (9)	0.015 (2)	0.14 (2)	10.2 (1)	0.014 (2)	0.15 (3)	11.7 (6)	0.013 (3)
SiO <sub>2</sub>	43 (2)	55.8 (6)	0.770 (9)	42.8 (2)	53.5 (2)	0.799 (5)	42.5 (2)	50 (3)	0.850 (7)
CaO	0.13 (2)	6.0 (5)	0.022 (3)	0.07 (6)	4.56 (5)	0.02 (1)	0.12 (4)	6.1 (1)	0.020 (6)
TiO <sub>2</sub>					0.48 (2)			0.95 (6)	
CoO							0.79 (1)	0.715 (6)	1.1 (1)
GeO <sub>2</sub>								1.124 (8)	
BaO					0.98 (7)			1.00 (4)	
Total	101.0 (4)	99.3 (3)		100.5 (5)	99.5 (4)		100.1 (4)	99.4 (6)	
Trace elements by LA-ICPMS (ppm unless specified)									
<i>n</i>	5	2	—	3	9	—	8	7	—
Al <sub>2</sub> O <sub>3</sub> (wt%)	0.062 (5)	9.3 (2)	0.0067 (5)	0.074 (5)	9.2 (1)	0.0080 (6)	0.106 (1)	10.1 (3)	0.0105 (4)
CaO (wt%)	bdl	5.07 (5)	0.017 (5)	0.073 (4)	4.48 (8)	0.0164 (9)	0.11 (1)	5.5 (2)	0.021 (2)
Sc	26 (1)	212 (2)	0.124 (7)	40 (2)	324 (3)	0.123 (5)	46.5 (5)	349 (14)	0.134 (5)
Ti				220 (14)	2443 (47)	0.090 (6)	63.4 (8)	4288 (141)	0.0148 (5)
V	149 (18)	32.69 (8)	4.6 (5)	31 (2)	11 (2)	2.8 (5)	252 (3)	781 (13)	0.323 (7)
Mn				220 (2)	371 (3)	0.592 (8)	779 (4)	1421 (30)	0.55 (1)
Co	0.15 (3) <sup>§</sup>	0.09 (1)	1.7 (5)	bdl	2.1 (5)	0.9 (2)	6644 (258)	4628 (106)	1.44 (6)
Zn				bdl	11.9 (3)	0.66 (3)	250 (3)	352 (7)	0.71 (2)
Ge	< 0.27*	11 (1)	< 0.03	< 0.068*	15 (3)	< 0.005*	1409 (53)	9095 (113)	0.155 (6)
Sr				bdl	1687 (14)	5.44 (5) x 10 <sup>-5</sup>	0.2 (1)	1893 (53)	1.2 (7) x 10 <sup>-4</sup>
Y	52 (3)	9305 (26)	0.0056 (4)	bdl	2809 (29)	0.0060 (1)	21.7 (3)	3113 (125)	0.0070 (3)
Zr				bdl	1414 (12)	8.52 (7) x 10 <sup>-4</sup>	1.30 (7)	1602 (48)	8.1 (5) x 10 <sup>-4</sup>
Ba				bdl	7885 (121)				
Hf				bdl	1947 (21)	0.00116 (1)			
T Sc/Y**	1466 (53)			1491 (30)			1496 (37)		

454

455 Table 5. Continued.

	D2368-ii			C4444			D2413		
	Olivine	Melt	D <sup>ol/melt</sup>	Olivine	Melt	D <sup>ol/melt</sup>	Olivine	Melt	D <sup>ol/melt</sup>
	Major elements by EDS using a FE-SEM (wt%)								
<i>n</i>	5	5	—	6	8	—	8	8	—
MgO	56.7 (2)	28 (3)	2.0 (2)	57.2 (4)	36.6 (5)	1.56 (2)	57.2 (7)	30.5 (4)	1.87 (4)
Al <sub>2</sub> O <sub>3</sub>	0.18 (4)	11 (1)	0.016 (4)	0.14 (4)	7.4 (3)	0.019 (5)	0.17 (3)	9.9 (3)	0.03 (4)
SiO <sub>2</sub>	42.5 (2)	50.9 (8)	0.84 (1)	42.7 (2)	47.1 (3)	0.907 (6)	42.8 (6)	48.4 (7)	0.89 (2)
CaO	0.11 (2)	5.1 (6)	0.021 (5)	bdl	3.37 (8)	0.01 (2)	0.08 (6)	4.4 (1)	0.03 (4)
TiO <sub>2</sub>		0.91 (8)							
CoO	0.7 (2)	0.59 (3)	1.3 (3)						
GeO <sub>2</sub>		1.24 (7)							
BaO		1.0 (1)						1.39 (6)	
Total	100.3 (5)	99.11 (8)		100.0 (5)	96.3 (5)**		100 (1)	95 (1)**	
	Trace elements by LA-ICPMS (ppm unless specified)								
<i>n</i>	6	5	—	7	8	—	10	9	—
Al <sub>2</sub> O <sub>3</sub> (wt%)	0.105 (1)	9.74 (6)	0.0108 (1)	0.062 (4)	6.6 (2)	0.0094 (7)	0.081 (3)	8.8 (2)	0.0092 (4)
CaO (wt%)	0.10 (2)	4.51 (7)	0.022 (3)	0.062 (3)	3.14 (1)	0.020 (1)	0.08 (2)	4.0 (1)	0.020 (4)
P				42 (2)	64.4 (7)	0.66 (3)	53 (6)	181 (6)	0.29 (4)
Sc	46.8 (6)	336 (4)	0.140 (3)	26.0 (5)	170 (2)	0.153 (4)	42 (1)	304 (10)	0.139 (7)
Ti	65 (2)	4085 (46)	0.0159 (6)	3.0 (2)	52 (2)	0.057 (5)	23 (2)	3218 (46)	0.0071 (6)
V	257 (6)	741 (10)	0.347 (9)	4 (1)	919 (22)	0.004 (1)	2.2 (1)	765 (19)	0.0029 (2)
Cr				2.6 (2)	12.2 (3)	0.22 (2)	1.2 (2)	3 (5)	0.41 (9)
Mn	759 (8)	1394 (23)	0.54 (1)	8.9 (4)	25.4 (7)	0.35 (2)	632 (11)	1321 (39)	0.48 (2)
Fe				74 (7)	636 (24)	0.12 (1)	49 (5)	383 (10)	0.13 (1)
Co	5870 (340)	4058 (198)	1.4 (1)	22.6 (2)	22.2 (3)	1.01 (2)	3.52 (9)	2.72 (5)	1.29 (4)
Ni				359 (5)	175 (6)	2.05 (8)	45 (3)	16 (3)	2.8 (6)
Zn	255 (3)	343 (6)	0.74 (1)	17 (1)	33.6 (4)	0.52 (3)	253 (5)	336 (17)	0.75 (4)
Ge	1146 (50)	8780 (196)	0.131 (6)	1759 (36)	3090 (25)	0.57 (1)	1271 (32)	2176 (21)	0.58 (2)
Sr	0.14 (2)	1783 (15)	8 (1) x 10 <sup>-5</sup>	0.02 (3)	13.0 (4)	0.002 (2)	0.3 (3)	1594 (40)	2 (2) x 10 <sup>-4</sup>
Y	21.0 (2)	2939 (32)	0.0072 (1)	50 (1)	7239 (181)	0.0069 (2)	17.6 (7)	2627 (91)	0.0067 (4)
Zr	1.34 (7)	1530 (15)	0.00087 (5)	0.14 (3)	159 (3)	9 (2) x 10 <sup>-4</sup>	1.02 (9)	1336 (32)	7.7 (7) x 10 <sup>-4</sup>
Ba				bdl	12.8 (4)		0.5 (5)	7324 (184)	6 (7) x 10 <sup>-5</sup>
Hf				0.009 (3)	3.7 (1)	0.0025 (9)	2.2 (2)	1791 (35)	0.0013 (1)
T Sc/Y <sup>†</sup>	1500 (16)			1468 (24)			1484 (49)		

456 \*Maximum values reported for Ge in D2270 and D2357 are based on the lowest detection limit obtained from LA-ICPMS for the respective samples. *n* =  
457 number of analyses. bdl = below detection limit. Numbers in parentheses are one standard deviation on the last digit. \*\*EDS totals of C4444 and D2413 are  
458 slightly higher than the sum of the oxides; this is because 2-3 additional trace elements, that were included in the EDS analysis, are not reported in this table.

459 Where values are not given, the element wasn't included in the analysis. <sup>58</sup>Co in D2270 olivine was only analysed in n=4/5 spots. <sup>†</sup>Temperature (°C) calculated  
460 using the Sc/Y geothermometer of Mallmann and O'Neill (2013).  
461

462

463 We used the partition coefficients of Y and Sc as a check that olivine and melt equilibrated in  
 464 the experiments. The two-element distribution coefficient of Y and Sc was calibrated as a  
 465 geothermometer by Mallmann and O'Neill (2013). Calculated temperatures are listed in  
 466 Table 5 and are in all cases in good agreement with the nominal run temperature of 1500°C.

467 The Ge partition coefficient as a function of  $\log fO_2$  is shown in Figure 8. In the two most  
 468 reduced samples, Ge in olivine was below the detection limit of LA-ICPMS. The Ge  
 469 detection limit for D2357 was lower than for D2270, because D2357 contained larger crystals  
 470 and so a larger spot size could be used. Maximum partition coefficients for both samples  
 471 based on the detection limits are plotted in Figure 8 as downward pointing arrows.

472 The partition coefficient of Ge over the range in which the valence state of Ge changes can be  
 473 defined by relating the bulk partition coefficient of Ge ( $D_{\Sigma Ge}$ ) to the fraction of  $Ge^{4+}$  in the  
 474 sample ( $\frac{Ge^{4+}}{\Sigma Ge}$ ) and to the respective partition coefficients for each valence state ( $D_{Ge^{4+}}$  and  
 475  $D_{Ge^{2+}}$ ):

$$476 \quad D_{\Sigma Ge} = \frac{Ge^{4+}}{\Sigma Ge} \cdot D_{Ge^{4+}} + \left(1 - \frac{Ge^{4+}}{\Sigma Ge}\right) \cdot D_{Ge^{2+}} \quad \text{Equation 7}$$

477 Substituting Equation 5 into Equation 7 gives:

$$478 \quad D_{Ge(bulk)} = \frac{D_{Ge^{4+}} + D_{Ge^{2+}} \cdot 10^{-(0.5\Delta IW + \log K'')}}{1 + 10^{-(0.5\Delta IW + \log K'')}} \quad \text{Equation 8}$$

479 The partitioning results were fitted to Equation 8 to evaluate  $\log K''$ , which should be  
 480 consistent with the XANES results. For this fit,  $D_{Ge^{4+}}$  was set at 0.58(1). For  $D_{Ge^{2+}}$ , the fit is  
 481 insensitive to any value  $<0.005$ , and was set arbitrarily to 0.004; the precise value has  
 482 negligible effect on the value of  $\log K''$ , because  $\log K''$  controls only the position of the  
 483 sigmoid in  $\log fO_2$  space. For example, if  $D_{Ge^{2+}}$  was assumed to be two orders of magnitude  
 484 smaller, the fitted  $\log K''$  would change by 0.01, which is within the confidence interval on  
 485 the fitted value assuming  $D_{Ge^{2+}}$  is 0.004. The maximum and minimum  $fO_2$  estimates for  
 486 D2368-i and D2368-ii were used in the fit, and the calculated  $\log K''_{eq}$  ranges from -0.02(1)  
 487 to -0.37(1). This range is represented by the grey curve in Figure 8. These values are  
 488 reasonably consistent with those obtained by fitting the XANES data from glasses; for the  
 489 low-pressure and high-pressure datasets,  $\log K'' = 0.15(28)$  and  $0.52(63)$  respectively (Table  
 490 3 and Figure 9).

## 491 **4 Discussion**

### 492 **4.1 Evidence for Ge<sup>2+</sup> in high-temperature melts**

493 The interpretation that Ge<sup>2+</sup> is a stable species in high-temperature melts relies upon three  
494 assertions. These are: (1) that the XAS spectra provide evidence for Ge<sup>2+</sup>, which can be  
495 reliably distinguished from other oxidation states, particularly Ge<sup>0</sup>; (2) that exposure to the  
496 X-ray beam does not change the Ge speciation; and (3) that quenching the melt to glass does  
497 not change the Ge speciation.

498 Firstly, we must justify the interpretation that the low-*f*O<sub>2</sub> samples contain Ge<sup>2+</sup> and not Ge<sup>0</sup>.  
499 Hypothetically, Ge<sup>0</sup> might exist in the glasses either as nano-nuggets or as isolated atoms.  
500 However, the XAS spectra do not support the hypothesis that Ge<sup>0</sup> is the species present in the  
501 low-*f*O<sub>2</sub> samples. The spectra of the two Ge<sup>0</sup> standards have absorption edges at distinctly  
502 lower energies than the spectra of the low-*f*O<sub>2</sub> glasses (Figure 3, Figure S1), and the spectral  
503 shapes are very different (Figure 3). Attempts to reproduce the ‘Ge<sup>2+</sup>’ spectrum using a linear  
504 combination of Ge<sup>4+</sup> and Ge<sup>0</sup> fail (Figure S5), and attempts to reproduce the spectrum of a  
505 sample prepared at IW +0.5 using a combination Ge<sup>4+</sup> and Ge<sup>0</sup> are poor compared with fits  
506 that use the Ge<sup>4+</sup> and Ge<sup>2+</sup> spectra as end-members (Figure S6). We are therefore confident in  
507 assigning the spectra of the lowest-*f*O<sub>2</sub> glasses to be representative of a Ge<sup>2+</sup> spectrum,  
508 probably with a minor component of Ge<sup>4+</sup> (< 10%) as indicated by the sigmoidal fits (Figure  
509 5).

510 Next we must consider whether exposure to the X-ray beam may have altered the Ge  
511 speciation in the samples (a phenomenon known as ‘beam damage’). The first-order  
512 observation that glasses prepared at different *f*O<sub>2</sub>s but otherwise identical in composition  
513 gave different Ge spectra rules out beam damage as a major problem, but experience with  
514 XAS on sulfur species dissolved in silicate glasses has shown that some damage affecting the  
515 precise proportions of the different valence states may still occur (e.g., Métrich et al. 2009;  
516 Jugo et al. 2010). The evidence that this effect does not occur with Ge is the good fit obtained  
517 for the calculated Ge<sup>2+</sup>/Ge<sup>4+</sup> ratio as a function of *f*O<sub>2</sub> with the theoretical stoichiometry of  
518 the reaction as given by Equation 3, and shown in Figure 5. The beam damage in early XAS  
519 measurements on S<sup>2-</sup>/S<sup>6+</sup> ratios in silicate glasses produced marked deviations between the  
520 apparent speciation and the theoretical stoichiometry, as shown by Jugo et al. (2010). In  
521 addition, we checked for beam damage by recording two spectra consecutively at the same  
522 spot on samples prepared at IW -3 and IW -2.5. Each spectrum took ~30 min to acquire, and

523 we found no evidence for beam damage, as the spectra were similar, indicating that the  
524 speciation is not changing under the X-ray beam on the timescale of a scan.

525 Finally, we must consider whether the speciation of Ge might change upon quenching a melt  
526 to a glass through electron exchange reactions between Ge and other multivalent elements,  
527 such as Fe, for example via the reaction:  $\text{Ge}^{4+} + 2\text{Fe}^{2+} = \text{Ge}^{2+} + 2\text{Fe}^{3+}$ . This would be similar  
528 to the reaction between Fe and Cr oxidation states in silicate melts ( $\text{Fe}^{3+} + \text{Cr}^{2+} = \text{Fe}^{2+} + \text{Cr}^{3+}$ )  
529 that was documented by Berry et al. (2003b). Berry et al. (2003b) found that the reaction  
530 occurred too rapidly to quench. Although the glasses were nominally Fe-free, with no added  
531 trace elements other than Ni or Co, LA-ICPMS analysis indicated  $\sim 350 (\pm 70)$  ppm Fe in all  
532 samples, hence an electron exchange reaction could affect those samples with low Ge, such  
533 as the most reducing glasses, which contained only  $\sim 300$  to 400 ppm Ge. Again, the good  
534 agreement between observed and theoretical sigmoidal slope shown in Figure 5 argues  
535 against this possibility being a major problem, although this process may have had a small  
536 effect on our results, as discussed in the Section 4.2. The electron-exchange effect is not  
537 relevant to partitioning experiments, because the slow rate of chemical diffusion means that  
538 partition coefficients do not alter upon quenching. Therefore, the agreement between the  
539 partitioning data and the XANES data from the glasses suggests that the speciation of Ge  
540 does not change substantially upon quenching from a melt to a glass.

#### 541 4.2 Deviation of the results from the sigmoidal trend

542 In detail, the transition from  $\text{Ge}^{4+}$  to  $\text{Ge}^{2+}$  in our samples does not occur perfectly smoothly  
543 with  $f\text{O}_2$  (Figure 3), and this is reflected by the scatter around the sigmoid in Figure 5. The  
544 scatter is larger than that observed in similar studies (e.g. Cr, Berry and O'Neill, 2004; Eu,  
545 Burnham et al., 2015), and cannot be attributed to noise or energy drift in the spectra. Instead,  
546 these deviations are likely to result from the sample preparation techniques. We envision two  
547 possible processes that could explain the scatter.

548 Firstly, the 1-atm experiments depend on establishing a steady state between Ge acquired by  
549 the sample from the vapour of the source at the bottom of the silicate tube, and Ge lost by  
550 vaporization from the sample (Figure 2). Since the vapour species is  $\text{Ge}^{2+}\text{O}$  (Barton and Heil,  
551 1970), the preferential loss of  $\text{Ge}^{2+}$  might perturb the equilibrium between  $\text{Ge}^{2+}$  and  $\text{Ge}^{4+}$ . It  
552 is possible that the oxidation state of Ge in the glasses differs between rims and cores of the  
553 glass samples, but testing this was not possible at the XAS beamline because of the spatial

554 limitations of the incident beam. In any case, this explanation cannot account for the  
555 deviations from the sigmoid in the data from the high-pressure experiments.

556 Alternatively, the apparent effect of concentration seen in Figure 4 must be considered. The  
557 spectrum of sample E021213A containing ~300 ppm Ge and prepared in air, showed a  
558 shoulder at the same energy as the  $\text{Ge}^{2+}$  peak (Figure 4), which may reflect a small fraction of  
559  $\text{Ge}^{2+}$ . Linear combination fitting reproduces the spectrum well, with about 10%  $\text{Ge}^{2+}$  (see  
560 supplementary information, Figures S3 and S4), but  $\text{Ge}^{2+}$  is not expected to be stable at this  
561 high  $f\text{O}_2$ , and there is no evidence for  $\text{Ge}^{2+}$  in the other two samples that were prepared in air  
562 (which contained 2900-ppm and 2-wt% Ge; Figure 4). However, if a fixed amount (e.g., 30  
563 ppm) of  $\text{Ge}^{4+}$  were reduced to  $\text{Ge}^{2+}$  by an electron-exchange reaction with Fe during  
564 quenching, this would be clearly visible in the spectrum of the 300-ppm sample but not in the  
565 spectra of the 2900-ppm or 2-wt% samples. This explanation is quantitatively consistent with  
566 the stoichiometry of the electron exchange reaction ( $\text{Ge}^{4+} + 2\text{Fe}^{2+} = \text{Ge}^{2+} + 2\text{Fe}^{3+}$ ). In sample  
567 E021213A, we calculate that the melt would have contained 53(4) at.ppm  $\text{Fe}^{2+}$ , based on the  
568 parameterization of  $\text{Fe}^{3+}/\text{Fe}^{2+}$  as a function of oxygen fugacity from O'Neill et al. (2018),  
569 their Equation 9b. Upon quenching, the electron-exchange reaction could have produced  
570 27(4) at.ppm  $\text{Ge}^{2+}$ , which agrees well with our estimate of 28(6) at.ppm  $\text{Ge}^{2+}$  in the sample  
571 based on the XANES spectra. If this explanation is correct, it suggests that an electron-  
572 exchange reaction could have affected the other samples as well.

573 However, it is unlikely that the electron-exchange reaction went to completion in all samples.  
574 For example, the lowest- $f\text{O}_2$  sample (D120416) contains 550 at.ppm  $\text{Ge}^{2+}$  and 350 at.ppm  
575  $\text{Fe}^{2+}$ , therefore ~30% of the  $\text{Ge}^{2+}$  observed in the spectra could have been produced by the  
576 electron-exchange reaction. If we apply this logic to each sample and 'correct' the observed  
577  $\text{Ge}^{4+}/\Sigma\text{Ge}$  ratio accordingly, the sigmoidal trend changes dramatically and becomes  
578 inconsistent with the theoretical slope (Figure S7). Therefore, the electron-exchange process  
579 must not have significantly affected the samples. However, this does not rule out that the  
580 exchange reaction may occur to a small extent depending on its kinetics, which could  
581 modulate the  $\text{Ge}^{2+}/\Sigma\text{Ge}$  of the samples according to the interplay between these kinetics and  
582 the cooling rate. Given that the cooling rate on quenching likely varied among experiments  
583 because of the experimental set-up, it is possible that the electron exchange reaction could  
584 have affected each experiment differently.

### 585 4.3 The relative $fO_2$ of the $Ge^{4+}$ – $Ge^{2+}$ transition

586 As shown in Figure 5, our data follow the theoretical sigmoidal trend that is expected of the  
587 transition from  $Ge^{4+}$  to  $Ge^{2+}$  with decreasing  $fO_2$ . There is a small difference in the results  
588 from the different approaches to quantifying the spectra; approaches based on spectral  
589 features predict a small amount of  $Ge^{4+}$  (<10%) in the most reduced samples, whereas in the  
590 linear combination fitting approach, these samples are assumed to contain only  $Ge^{2+}$ .  
591 Therefore, we consider the results based on spectral features to be slightly more accurate.  
592 Using these results, the  $Ge^{4+}$ – $Ge^{2+}$  transition from  $Ge^{4+}/\Sigma Ge = 0.95$  to 0.05 is from IW +2.4  
593 to  $\Delta IW$  -2.8. This is supported by our olivine–melt partitioning data.

594 Whether the Ge valence state may be affected by pressure, temperature or composition is  
595 uncertain. The literature data are insufficient to resolve these effects, other than to say that  
596  $Ge^{2+}$  appears to be dominant in metal-silicate partitioning experiments below IW and at least  
597 up to 3 GPa and 2200°C (Figure 1). In the present study, we ran experiments at 1200 °C and  
598 1500 °C, 1 atmosphere and 1 GPa, using three CMAS compositions that vary in their NBO/T  
599 from 0.5 and 0.6 for AnDi and CMAS7G respectively, to 1.3–1.5 for the melt composition in  
600 the CMAS40 partitioning experiments, D2368-i and -ii. Our data from all experimental  
601 conditions gave consistent results within error (see Figure 9).

### 602 4.4 Systematics of olivine-melt trace-element partition coefficients

603 Partition coefficients for a number of trace elements are plotted as a function of their ionic  
604 radii in Figure 10. These data are from two representative partitioning experiments, one  
605 conducted at high  $fO_2$  (IW +8.6) and one at low  $fO_2$  (IW -7.2). If partitioning between phases  
606 was at equilibrium then the values for elements of the same charge that occupy the same  
607 crystallographic site should fall on a parabola (i.e. a lattice-strain model; Blundy and Wood,  
608 1994; Brice, 1975).

609 We were able to fit a lattice strain model to most of the 2+ cations: Mg, Zn, Mn, Ca and Sr  
610 (fit parameters are given in the supplementary information, Table S7). The partitioning of Co  
611 is not adequately described by the lattice-strain model because of crystal field effects (Wood  
612 and Blundy, 2014) and so this cation was not included in the fits. The multivalent element  
613 Mn is included, because at the conditions of these experiments, it is expected to be  
614 predominantly in the 2+ valence state, based on our unpublished XANES spectra of synthetic  
615 MORB equilibrated at a range of  $fO_2$  values. Partition coefficients for Be were calculated

616 using Equation 1 in Burnham and O'Neill (2016) in order to better constrain the fit, although  
617 the samples in this study contained no Be.

618 It was not possible to fit lattice strain models to the 3+ cations, because  $\text{Al}^{3+}$  substitutes on  
619 both tetrahedral and octahedral sites, leaving only  $\text{Sc}^{3+}$  and  $\text{Y}^{3+}$ , and at least three elements  
620 are required to constrain a parabola. Likewise, no fit was made for the 4+ cations;  $\text{Si}^{4+}$  and  
621  $\text{Ge}^{4+}$  occupy the tetrahedral site, but  $\text{Hf}^{4+}$  and  $\text{Zr}^{4+}$  are too large for this site (Jollands et al.,  
622 2014), while  $\text{Ti}^{4+}$  may substitute either for Si on tetrahedral sites or on octahedral sites by a  
623 vacancy-coupled substitution (Hermann et al., 2005; Jollands et al. 2016a).

624 The success of the lattice strain model is based on its ability to account for the partition  
625 coefficients of elements forming cations with spherically symmetric electron configurations.  
626 These include cations with a noble-gas electron configuration (e.g., the alkalis and the  
627 alkaline earths) and the REEs, but not, as noted above, cations of the transition metals with  
628 3d orbitals like  $\text{Co}^{2+}$ . In order to assess whether the partitioning of  $\text{Ge}^{2+}$ , with its lone pair of  
629 electrons and implied covalent bonding character, is also described by the lattice strain  
630 model, we need an estimate of the ionic radii of  $\text{Ge}^{2+}$ . Shannon (1976) lists a value for the  
631 radius of  $\text{Ge}^{2+}$  in octahedral coordination ( $r_{\text{oct}}$ ) of 0.73 Å, which was estimated from the  
632 ionisation potential according to a suggestion by Ahrens (1952) of dubious validity, but does  
633 not give a value for  $r_{\text{tet}}$  of  $^{[4]}\text{Ge}^{2+}$ , despite  $\text{Ge}^{2+}$  being only known in tetrahedral coordination  
634 (albeit distorted).

635 Ionic radii of the type compiled by Shannon (1976) may be estimated from our EXAFS  
636 results if we subtract from the bond length the ionic radius of  $\text{O}^{2-}$ . The ionic radius of  $\text{O}^{2-}$   
637 depends on its coordination number, being 1.38 and 1.40 Å in tetrahedral and octahedral  
638 coordination (Shannon, 1976). If we assume that the  $\text{O}^{2-}$  anions in silicate melts have an  
639 average coordination between these extremes, we may assign an ionic radius of 1.39(1). With  
640 this value, the ionic radii are estimated as 0.36(2) Å for  $\text{Ge}^{4+}$  and 0.50(3) Å for  $\text{Ge}^{2+}$ . The  
641 former compares quite well to the value listed in Shannon (1976) for  $\text{Ge}^{4+}$  in tetrahedral  
642 coordination ( $r_{\text{tet}}$ ) of 0.39 Å, and with the value of 0.38 Å for  $\text{Ge}^{4+}$  in the tetrahedral sites of  
643 oxide spinels (O'Neill and Navrotsky 1983). The latter is smaller than that of any other  
644 divalent cation (Co, Fe, Mg, Mn, Ni and Zn), apart from Be, which has a radius of 0.27 Å in  
645 tetrahedral coordination. We can then estimate  $r_{\text{oct}}$  for  $\text{Ge}^{2+}$  given that the ratio  $r_{\text{tet}}/r_{\text{oct}}$  of the  
646 above divalent cations is 0.80(1), suggesting  $r_{\text{oct}}$  for  $\text{Ge}^{2+}$  should be 0.63(4) Å, considerably  
647 smaller than the guess given in Shannon (1976) of 0.73 Å.

648 The value of  $D_{\text{Ge}^{2+}}$  falls well below the parabola for 2+ cations in octahedral coordination in  
649 the lattice strain model (Figure 9). One explanation is that the model is not applicable to  
650 cations like  $\text{Ge}^{2+}$  with its asymmetric arrangement of bonding electrons. Another is that  $\text{Ge}^{2+}$   
651 substitutes onto the tetrahedral site, despite its relatively large size for  $\text{Si}^{4+}$ -containing sites  
652 and its propensity for distorted tetrahedral coordination due to its lone pair. This substitution  
653 would require charge balancing, for example by an octahedral-site cation vacancy, but the  
654 even smaller  $\text{Be}^{2+}$  does not substitute into tetrahedral sites in this way (Jollands et al. 2016b).  
655 The important point is that  $\text{Ge}^{2+}$ , unlike either  $\text{Ge}^{4+}$  or the other smaller divalent cations  
656 (except  $\text{Be}^{2+}$ ) is highly incompatible in olivine, and its small size and bonding preferences for  
657 distorted tetrahedral coordination argue that it may similarly be highly incompatible in other  
658 rock-forming silicates.

## 659 4.5 Implications

### 660 4.5.1 Models of Earth's core formation

661 Our results support the idea that  $\text{Ge}^{2+}$  was the dominant species at the  $f\text{O}_2$ s prevalent during  
662 the formation of Earth's core ( $\sim\text{IW}-2$ ; Wood et al., 2006), if metal segregation occurred at  
663 low pressure. Whether this applies to the very high pressure expected at the bottom of a lunar  
664 magma ocean requires further work.

665 Recent work has attempted to use Ge isotopes to trace the core-forming process. Measured  
666 values of Ge isotopic composition of mantle silicates and magmatic iron meteorites (a proxy  
667 for the Earth's core) indicates a positive  $\Delta^{74/70}\text{Ge}$  fractionation factor, yet theoretical  
668 predictions yield a negative value (Luais, 2012; Rouxel and Luais, 2017). Luais (2012)  
669 suggested that the discrepancy arose because the isotopic composition measured for silicate  
670 materials is a poor estimate for the bulk silicate Earth, due to the lack of samples from the  
671 deep or ancient mantle. However, the calculations used to predict fractionation factors  
672 depend on oxidation state, coordination number and bond lengths (Li et al., 2009), which  
673 assumed  $\text{Ge}^{4+}$  in the silicate, and not  $\text{Ge}^{2+}$ .

### 674 4.5.2 Ge in lunar magmatism

675 The  $f\text{O}_2$  at which lunar basalts crystallised, as well as the  $f\text{O}_2$  of the lunar mantle, is thought  
676 to be at or below IW (Wieczorek et al., 2006) and thus  $\text{Ge}^{2+}$  is likely to be the major species  
677 on the Moon. Ge is very depleted in the Moon, but is enriched in KREEP basalts (Dickinson  
678 et al., 1989; Haskin and Warren, 1991). KREEP refers to the last, highly evolved magma that

679 crystallised from the lunar magma ocean, which was enriched in K, REE and P. This material  
680 was then sampled by the ‘KREEP basalts’, which erupted onto the lunar surface. The unusual  
681 enrichment of Ge in KREEP was a puzzle to Dickinson et al. (1989), because, working with a  
682 partition coefficient between silicate minerals and melt of  $\sim 0.7$  for  $\text{Ge}^{4+}$  (Capobianco and  
683 Watson, 1982), there would be very little Ge enrichment due to processes like fractional  
684 crystallisation. Dickinson et al. (1989) therefore proposed a model involving lunar mantle  
685 metasomatism, which transported and concentrated Ge. The results presented here indicate  
686 that  $\text{Ge}^{2+}$  is probably the dominant oxidation state on the Moon, and unlike  $\text{Ge}^{4+}$ , it is highly  
687 incompatible.  $\text{Ge}^{2+}$  may therefore be enriched in KREEP simply as a result of its  
688 incompatibility.

689 The reverse side of this particular coin is that Ge, as a highly incompatible element under  
690 lunar redox conditions, should be greatly depleted in those lunar basalts derived from the  
691 remelting of magma ocean cumulates. This may contribute to the great depletion of Ge in  
692 lunar basalts relative to terrestrial basalts, of a factor of 200 (O’Neill 1991a), although this  
693 does not invalidate the traditional view that volatility and partitioning into the lunar core are  
694 important factors.

## 695 **5 Conclusion**

696 Germanium has not been analysed routinely with other trace elements in many geochemical  
697 studies, because little variation in Ge concentrations is observed in crustal and mantle rocks.  
698 This homogeneity is a result of the mineral–silicate melt partition coefficients of  $\text{Ge}^{4+}$  being  
699 close to unity for rock-forming silicates, preventing any significant fractionation during  
700 magmatic processes in the relatively oxidised conditions of the present-day upper mantle and  
701 crust of the Earth. However, in the more reducing conditions relevant to the Moon and most  
702 achondrite meteorite parent bodies,  $\text{Ge}^{2+}$  becomes stable relative to  $\text{Ge}^{4+}$ , with the transition  
703 from 95%  $\text{Ge}^{4+}$  to 95%  $\text{Ge}^{2+}$  occurring over the range in relative  $f\text{O}_2$  from IW +2.4 to IW -  
704 2.8. The example of  $\text{Ge}^{2+}$  suggests that the lattice-strain model for mineral–melt partition  
705 coefficients may not apply to cations with lone-pair orbitals forming covalent bonds, and in  
706 such cases ionic radii from Shannon (1976) may be a misleading indicator of the geochemical  
707 properties of the cation. Our olivine–melt partitioning experiments show that  $\text{Ge}^{2+}$  does not  
708 behave like the other smaller divalent cations (Mg, Mn, Fe, Co, Ni or Zn); unlike these  
709 divalent cations and also  $\text{Ge}^{4+}$ ,  $\text{Ge}^{2+}$  is highly incompatible in olivine. To judge from its  
710 crystal-chemical properties, namely its ionic radii in either octahedral coordination (too small

711 for Mg-containing sites) or tetrahedral co-ordination (too large for Si-containing sites), and  
712 its propensity for triangular pyramidal coordination and the covalent bonding implied by that  
713 stereochemistry, Ge<sup>2+</sup> will also be highly incompatible all other rock-forming silicates or  
714 oxides. Therefore the magmatic geochemistry of Ge in extraterrestrial rocks will be very  
715 different from its behaviour on Earth.

## 716 **Acknowledgements**

717 The authors acknowledge the scientific and technical assistance of the Australian Microscopy  
718 and Microanalysis Research Facility at the Centre of Advanced Microscopy, Australian  
719 National University. The spectroscopy part of this research was undertaken at the XAS  
720 beamline of the Australian Synchrotron, which is part of ANSTO. Peter Kappen, Bernt  
721 Johannessen and Jeremy Wykes are thanked for technical assistance at the beamline. Mark  
722 Ridgway is thanked for providing Ge<sup>0</sup> standards. Jung-Woo Park, Mike Jollands, Peter  
723 Tollan, James Tolley and Robert Rapp are thanked for technical assistance with LA-ICPMS  
724 and EPMA. The authors acknowledge an anonymous reviewer whose feedback was very  
725 useful in improving the manuscript. HON gratefully acknowledges funding from the  
726 Australian Research Council through grant FL130100066.

727

## 728 **References**

- 729 Ahrens, L.H., 1952. The use of ionization potentials Part 1. Ionic radii of the elements.  
730 *Geochim. Cosmochim. Acta* 2, 155–169. doi:10.1016/0016-7037(52)90004-5
- 731 Barton, L., Heil, C.A., 1970. The reduction of germanium dioxide with graphite at high  
732 temperatures. *J. Less-Common Met.* 22, 11–17. doi:10.1016/0022-5088(70)90171-2
- 733 Belissont, R., Muñoz, M., Boiron, M.-C., Luais, B., Mathon, O., 2016. Distribution and  
734 oxidation state of Ge, Cu and Fe in sphalerite by  $\mu$ -XRF and K-edge  $\mu$ -XANES: Insights  
735 into Ge incorporation, partitioning and isotopic fractionation. *Geochim. Cosmochim.*  
736 *Acta* 177, 298–314. doi:10.1016/j.gca.2016.01.001
- 737 Bernstein, L.R., 1985. Germanium geochemistry and mineralogy. *Geochim. Cosmochim.*  
738 *Acta* 49, 2409–2422. doi:10.1016/0016-7037(85)90241-8
- 739 Berry, A.J., O'Neill, H.St.C., 2004. A XANES determination of the oxidation state of  
740 chromium in silicate glasses. *Am. Mineral.* 89, 790–798. doi:10.2138/am-2004-5-613
- 741 Berry, A.J., O'Neill, H.St.C., Jayasuriya, K.D., Campbell, S.J., Foran, G.J., 2003a. XANES  
742 calibrations for the oxidation state of iron in a silicate glass. *Am. Mineral.* 88, 967–977.  
743 doi:10.2138/am-2003-0704

- 744 Berry, A.J., Shelley, J.M.G., Foran, G.J., O'Neill, H.St.C., Scott, D.R. (2003b). A furnace  
745 design for XANES spectroscopy of silicate melts under controlled oxygen fugacities and  
746 temperatures to 1773 K. *J. Synchrotron. Radiat.*, 10, 332-336.  
747 doi: 10.1107/S0909049503007556
- 748 Blundy, J., Wood, B., 1994. Prediction of crystal–melt partition coefficients from elastic  
749 moduli. *Nature* 372, 452–454. doi:10.1038/372452a0
- 750 Bonnet, J., Cauzid, J., Testemale, D., Kieffer, I., Proux, O., Lecomte, A., Bailly, L., 2017.  
751 Characterization of germanium speciation in sphalerite (ZnS) from central and eastern  
752 Tennessee, USA, by X-ray absorption spectroscopy. *Minerals* 7, 79.  
753 doi:10.3390/min7050079
- 754 Brice, J.C.C., 1975. Some thermodynamic aspects of the growth of strained crystals. *J. Cryst.*  
755 *Growth* 28, 249–253. doi:10.1016/0022-0248(75)90241-9
- 756 Burnham, A.D., Berry, A.J., Halse, H.R., Schofield, P.F., Cibin, G., Mosselmans, J.F.W.,  
757 (2015) The oxidation state of europium in silicate melts as a function of oxygen  
758 fugacity, composition and temperature. *Chem. Geol.* 411:248–259. doi:  
759 10.1016/j.chemgeo.2015.07.002
- 760 Burnham, A.D., O'Neill, H.St.C., 2016. The effect of melt composition on mineral–melt  
761 partition coefficients: The case of beryllium. *Chem. Geol.* 442, 139–147.  
762 doi:10.1016/j.chemgeo.2016.09.012
- 763 Capobianco, C.J., Drake, M.J., De'Aro, J., 1999. Siderophile geochemistry of Ga, Ge, and  
764 Sn: cationic oxidation states in silicate melts and the effect of composition in iron–nickel  
765 alloys. *Geochim. Cosmochim. Acta* 63, 2667–2677. doi:10.1016/S0016-7037(99)00085-  
766 X.
- 767 Capobianco, C.J., Watson, E.B., 1982. Olivine/silicate melt partitioning of germanium: an  
768 example of a nearly constant partition coefficient. *Geochim. Cosmochim. Acta* 46, 235–  
769 240. doi:10.1016/0016-7037(82)90250-2
- 770 Cempírek, J., Groat, L.A., 2013. Note on the formula of brunogeierite and the first bond-  
771 valence parameters for Ge<sup>2+</sup>. *J. Geosci.* 58, 71–74. doi:10.3190/jgeosci.130
- 772 Cook, N., Etschmann, B., Ciobanu, C., Geraki, K., Howard, D., Williams, T., Rae, N., Pring,  
773 A., Chen, G., Johannessen, B., Brugger, J., 2015. Distribution and substitution  
774 mechanism of Ge in a Ge-(Fe)-bearing sphalerite. *Minerals* 5, 117–132.  
775 doi:10.3390/min5020117
- 776 Dickinson, T., Taylor, G.J., Keil, K., Bild, R.W., 1989. Germanium abundances in lunar  
777 basalts: Evidence of mantle metasomatism? in: *Proceedings of the 19th Lunar and*  
778 *Planetary Science Conference.* pp. 189–198.
- 779 Ertel, W., O'Neill, H.St.C., Sylvester, P.J., Dingwell, D.B., & Spettel, B. (2001). The  
780 solubility of rhenium in silicate melts: implications for the geochemical properties of  
781 rhenium at high temperatures. *Geochim. Cosmochim. Acta* 65, 2161-2170.  
782 doi: 10.1016/S0016-7037(01)00582-8

- 783 Frost, R.B., 1991. Introduction to oxygen fugacity and its petrologic importance. Rev.  
784 Mineral. 25, 1–9.
- 785 Haskin, L., Warren, P., 1991. Lunar chemistry, in: Heiken, G.H., Vaniman, D.T., French,  
786 B.M. (Eds.), Lunar Sourcebook: A User's Guide to the Moon. Cambridge University  
787 Press, pp. 357–474.
- 788 Hermann, J., O'Neill, H.S., Berry, A.J., 2005. Titanium solubility in olivine in the system  
789 TiO<sub>2</sub>-MgO-SiO<sub>2</sub>: No evidence for an ultra-deep origin of Ti-bearing olivine. Contrib.  
790 Mineral. Petrol. 148, 746–760. doi:10.1007/s00410-004-0637-4
- 791 Hillgren, V.J., Drake, M.J., Rubie, D.C., 1996. High pressure and high temperature metal-  
792 silicate partitioning of siderophile elements: The importance of silicate liquid  
793 composition. Geochim. Cosmochim. Acta 60, 2257–2263. doi:10.1016/0016-  
794 7037(96)00079-8
- 795 Holzheid, A., Kegler, P., Frost, D., Rubie, D.C., Palme, H., 2007. Partitioning behaviour of  
796 Copper and Germanium: implications for terrestrial core formation scenarios, in: 38th  
797 Lunar and Planetary Science Conference. p. 2090.
- 798 Holzheid, A., Palme, H., Chakraborty, S., 1997. The activities of NiO, CoO and FeO in  
799 silicate melts. Chem. Geol. 139, 21–38. doi:10.1016/S0009-2541(97)00030-2
- 800 Ishida, K., Nishizawa, T., 1991. The Co-Ge (cobalt-germanium) system. J. Phase Equilibria  
801 12, 77–83. doi:10.1007/BF02663679
- 802 Jana, D., Walker, D., 1997a. The impact of carbon on element distribution during core  
803 formation. Geochim. Cosmochim. Acta 61, 2759–2763. doi:10.1016/S0016-  
804 7037(97)00091-4
- 805 Jana, D., Walker, D., 1997b. The influence of silicate melt composition on distribution of  
806 siderophile elements among metal and silicate liquids. Earth Planet. Sci. Lett. 150, 463–  
807 472. doi:10.1016/S0012-821X(97)00079-4
- 808 Jollands, M.C., O'Neill, H.St.C., Hermann, J., 2014. The importance of defining chemical  
809 potentials, substitution mechanisms and solubility in trace element diffusion studies: the  
810 case of Zr and Hf in olivine. Contrib. Mineral. Petrol. 168, 1055. doi:10.1007/s00410-  
811 014-1055-x
- 812 Jollands, M.C., Hermann, J., O'Neill, H.St.C., Spandler, C., Padrón-Navarta, J.A., 2016a.  
813 Diffusion of Ti and some divalent cations in olivine as a function of temperature,  
814 oxygen fugacity, chemical potentials and crystal orientation. J. Petrol., 57(10), 1983-  
815 2010. doi:10.1093/petrology/egw067
- 816 Jollands, M.C., Burnham, A.D., O'Neill, H.St.C., Hermann, J., Qian, Q., 2016b. Beryllium  
817 diffusion in olivine: a new tool to investigate timescales of magmatic processes. Earth  
818 Planet. Sci. Lett., 450, 71-82. 10.1016/j.epsl.2016.06.028
- 819 Jugo, P.J., Wilke, M., Botcharnikov, R.E., 2010. Sulfur K-edge XANES analysis of natural  
820 and synthetic basaltic glasses: implications for S speciation and S content as function of  
821 oxygen fugacity. Geochim. Cosmochim. Acta 74, 5926-5938. doi:  
822 10.1016/j.gca.2010.07.022

- 823 Kegler, P., Holzheid, A., 2011. Determination of the formal Ge-oxide species in silicate melts  
824 at oxygen fugacities applicable to terrestrial core formation scenarios. *Eur. J. Mineral.*  
825 23, 369–378. doi:10.1127/0935-1221/2011/0023-2097
- 826 Laubengayer, A.W., Morton, D.S., 1932. Germanium. XXXIX. The polymorphism of  
827 germanium dioxide. *J. Am. Chem. Soc.* 54, 2303–2320. doi:10.1021/ja01345a019
- 828 Lee, C.-S., Weng, S.-F. 2008. A quaternary germanium (II) phosphate, Na[Ge<sub>4</sub>(PO<sub>4</sub>)<sub>3</sub>]. *Acta*  
829 *Crystallographica Section E: Structure Reports Online*, 64(3), i17.  
830 doi: 10.1107/S1600536808003231
- 831 Li, X., Zhao, H., Tang, M., Liu, Y., 2009. Theoretical prediction for several important  
832 equilibrium Ge isotope fractionation factors and geological implications. *Earth Planet.*  
833 *Sci. Lett.* 287, 1–11. doi:10.1016/j.epsl.2009.07.027
- 834 Luais, B., 2012. Germanium chemistry and MC-ICPMS isotopic measurements of Fe-Ni, Zn  
835 alloys and silicate matrices: insights into deep Earth processes. *Chem. Geol.* 334, 295–  
836 311. doi:10.1016/j.chemgeo.2012.10.017
- 837 Mallmann, G., O'Neill, H.St.C., 2013. Calibration of an empirical thermometer and  
838 oxybarometer based on the partitioning of Sc, Y and V between olivine and silicate  
839 melt. *J. Petrol.* 54, 933–949. doi:10.1093/petrology/egt001
- 840 Métrich, N., Berry, A.J., O'Neill, H.St.C., Susini, J., 2009. The oxidation state of sulfur in  
841 synthetic and natural glasses determined by X-ray absorption spectroscopy. *Geochim.*  
842 *Cosmochim. Acta* 73, 2382-2399. doi: 10.1016/j.gca.2009.01.025
- 843 Miller, L.A., O'Neill, H.S., Berry, A.J., Glover, C.J., 2019. The oxidation state and  
844 coordination environment of antimony in silicate glasses. *Chem. Geol.* 524, 283–294.  
845 doi:10.1016/j.chemgeo.2019.06.017.
- 846 Nash, A., Nash, P., 1987. The Ge–Ni (Germanium-Nickel) system. *Bull. Alloy Phase*  
847 *Diagrams* 8, 255–264. doi:10.1007/BF02874917
- 848 Norris, C.A., Wood, B.J., 2017. Earth's volatile contents established by melting and  
849 vaporization. *Nature* 549, 507–510. doi:10.1038/nature23645
- 850 O'Neill, H.St.C., 1991a. The origin of the Moon and the early history of the Earth—a  
851 chemical model. Part 1: The Moon. *Geochim. Cosmochim. Acta* 55, 1135–1157.  
852 doi:10.1016/0016-7037(91)90168-5
- 853 O'Neill, H.St.C., 1991b. The origin of the Moon and the early history of the Earth—a  
854 chemical model. Part 2: The Earth. *Geochim. Cosmochim. Acta* 55, 1159–1172.  
855 doi:/10.1016/0016-7037(91)90169-6
- 856 O'Neill, H.S., 2005. A method for controlling alkali-metal oxide activities in one-atmosphere  
857 experiments and its application to measuring the relative activity coefficients of NaO<sub>0.5</sub>  
858 in silicate melts. *Am. Mineral.* 90, 497–501. doi:10.2138/am.2005.1792.
- 859

- 860 O'Neill, H.St.C., Berry, A.J., 2006. Activity coefficients at low dilution of CrO, NiO and  
861 CoO in silicate melts in the system CaO-MgO-Al<sub>2</sub>O<sub>3</sub>-SiO<sub>2</sub> at 1400 °C: using the  
862 thermodynamic behaviour of transition metal oxides in silicate melts to probe their  
863 structure. *Chem. Geol.* 231, 77-89. doi:10.1016/j.chemgeo.2006.01.004
- 864 O'Neill, H.St.C., Eggins, S.M., 2002. The effect of melt composition on trace element  
865 partitioning: an experimental investigation of the activity coefficients of FeO, NiO,  
866 CoO, MoO<sub>2</sub> and MoO<sub>3</sub> in silicate melts. *Chem. Geol.* 186, 151–181. doi:10.1016/S0009-  
867 2541(01)00414-4
- 868 O'Neill, H.St.C., Navrotsky, A., 1983. Simple spinels: crystallographic parameters, cation  
869 radii, lattice energies, and cation distribution. *Am. Mineral.* 68, 181-194.
- 870 O'Neill, H.St.C., Nell, J., 1997. Gibbs free energies of formation of RuO<sub>2</sub>, IrO<sub>2</sub>, and OsO<sub>2</sub>: a  
871 high-temperature electrochemical and calorimetric study. *Geochim. Cosmochim. Acta*  
872 61, 5279–5293. doi:10.1016/S0016-7037(97)00317-7
- 873 O'Neill, H.St.C., Pownceby, M.I., 1993. Thermodynamic data from redox reactions at high  
874 temperatures. I. An experimental and theoretical assessment of the electrochemical  
875 method using stabilized zirconia electrolytes, with revised values for the Fe–“FeO”, Co–  
876 CoO, Ni–NiO and Cu–Cu<sub>2</sub>O oxygen buffers, and new data for the W–WO<sub>2</sub> buffer.  
877 *Contrib. Mineral. Petrol.* 114, 296–314. doi: 10.1007/BF01046533
- 878 O'Neill, H.St.C., Berry, A.J., & Mallmann, G. 2018. The oxidation state of iron in Mid-Ocean  
879 Ridge Basaltic (MORB) glasses: implications for their petrogenesis and oxygen  
880 fugacities. *Earth and Planetary Science Letters*, 504, 152-162.  
881 doi: 10.1016/j.epsl.2018.10.002
- 882 Pugsley, A.J., Bull, C.L., Sella, A., Sankar, G., McMillan, P.F., 2011. XAS/EXAFS studies  
883 of Ge nanoparticles produced by reaction between Mg<sub>2</sub>Ge and GeCl<sub>4</sub>. *J. Solid State*  
884 *Chem.* 184, 2345–2352. doi:10.1016/j.jssc.2011.06.020
- 885 Ravel, B., Newville, M., 2005. ATHENA, ARTEMIS, HEPHAESTUS: data analysis for X-  
886 ray absorption spectroscopy using IFEFFIT. *J. Synchrotron Radiat.* 12, 537–541.  
887 doi:10.1107/S0909049505012719
- 888 Ridgway, M.C., Azevedo, G. de M., Glover, C.J., Elliman, R.G., Llewellyn, D.J., Cheung,  
889 A., Johannessen, B., Brett, D.A., Foran, G.J., 2004. EXAFS characterisation of Ge  
890 nanocrystals in silica. *Nucl. Instrum. Methods Phys. Res. B* 218, 421–426.  
891 doi:10.1016/j.nimb.2004.01.004
- 892 Righter, K., King, C., Danielson, L., Pando, K., Lee, C.T., 2011. Experimental determination  
893 of the metal/silicate partition coefficient of Germanium: implications for core and  
894 mantle differentiation. *Earth Planet. Sci. Lett.* 304, 379–388.  
895 doi:10.1016/j.epsl.2011.02.015
- 896 Righter, K., Nickodem, K., Pando, K., Danielson, L., Boujibar, A., Righter, M., Lapen, T.J.,  
897 2017. Distribution of Sb, As, Ge, and In between metal and silicate during accretion and  
898 core formation in the Earth. *Geochim. Cosmochim. Acta* 198, 1–16.  
899 doi:10.1016/j.gca.2016.10.045

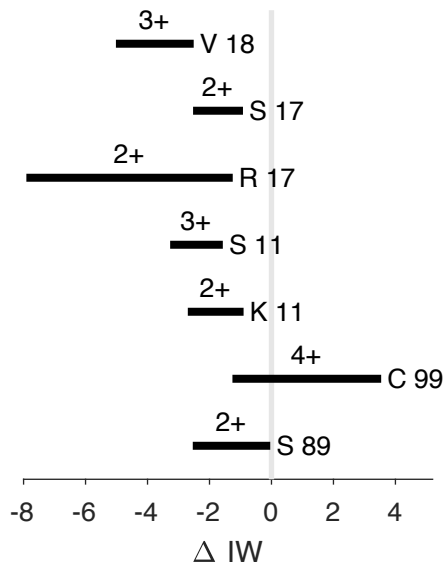
- 900 Rosenberg, E., 2008. Germanium: environmental occurrence, importance and speciation.  
901 Rev. Environ. Sci. Bio/Technology 8, 29–57. doi:10.1007/s11157-008-9143-x
- 902 Rouxel, O.J., Luais, B., 2017. Germanium isotope geochemistry. Rev. Mineral. Geochemistry  
903 82, 601–656. doi:10.2138/rmg.2017.82.14
- 904 Schmitt, W., Palme, H., Wänke, H., 1989. Experimental determination of metal/silicate  
905 partition coefficients for P, Co, Ni, Cu, Ga, Ge, Mo, and W and some implications for  
906 the early evolution of the Earth. Geochim. Cosmochim. Acta 53, 173–185.  
907 doi:10.1016/0016-7037(89)90284-6
- 908 Shannon, R.D., 1976. Revised effective ionic radii and systematic studies of interatomic  
909 distances in halides and chalcogenides. Acta Crystallogr. A32, 751–767.  
910 doi:10.1107/S0567739476001551
- 911 Siebert, J., Corgne, A., Ryerson, F.J., 2011. Systematics of metal–silicate partitioning for  
912 many siderophile elements applied to Earth’s core formation. Geochim. Cosmochim.  
913 Acta 75, 1451–1489. doi:10.1016/j.gca.2010.12.013
- 914 Smith, G.S., Isaacs, P.B., 1964. The crystal structure of quartz-like GeO<sub>2</sub>. Acta Crystallogr.  
915 17, 842–846. doi: 10.1107/S0365110X64002262
- 916 Sossi, P. A., Klemme, S., O'Neill, H.St.C., Berndt, J., Moynier, F., 2019. Evaporation of  
917 moderately volatile elements from silicate melts: experiments and theory. Geochim.  
918 Cosmochim. Acta 260, 204–231. doi: 10.1016/j.gca.2019.06.021
- 919 Steenstra, E.S., Rai, N., Knibbe, J.S., Lin, Y.H., van Westrenen, W., 2016. New geochemical  
920 models of core formation in the Moon from metal-silicate partitioning of 15 siderophile  
921 elements. Earth Planet. Sci. Lett. 441, 1–9. doi:10.1016/j.gca.2016.01.002
- 922 Steenstra, E.S., Sitabi, A.B., Lin, Y.H., Rai, N., Knibbe, J.S., Berndt, J., Matveev, S., van  
923 Westrenen, W., 2017. The effect of melt composition on metal-silicate partitioning of  
924 siderophile elements and constraints on core formation in the angrite parent body.  
925 Geochim. Cosmochim. Acta 212, 62–83. doi: 10.1016/j.epsl.2016.02.028
- 926 Vogel, A.K., Jennings, E.S., Laurenz, V., Rubie, D.C., Frost, D.J., 2018. The dependence of  
927 metal-silicate partitioning of moderately volatile elements on oxygen fugacity and Si  
928 contents of Fe metal: implications for their valence states in silicate liquids. Geochim.  
929 Cosmochim. Acta 237, 275–293. doi:10.1016/j.gca.2018.06.022
- 930 Walker, D., Norby, L., Jones, J.H., 1993. Superheating effects on metal-silicate partitioning  
931 of siderophile elements. Science 262, 1858–1861. doi:10.1126/science.262.5141.1858
- 932 Wiczorek, M.A., Jolliff, B.L., Khan, A., Pritchard, M.E., Weiss, B.P., Williams, J.G., Hood,  
933 L.L., Richter, K., Neal, C.R., Shearer, C.K., McCallum, I.S., Tompkins, S., Hawke,  
934 B.R., Peterson, C., Gillis, J.J., Bussey, B., 2006. The constitution and structure of the  
935 lunar interior. Rev. Mineral. Geochem. 60, 221–364. doi:10.2138/rmg.2006.60.3
- 936 Wong, J., Lytle, F.W., Messmer, R.P., Maylotte, D.H., 1984. K-edge absorption spectra of  
937 selected vanadium compounds. Phys. Rev. B 30, 5596–5610.  
938 doi:10.1103/PhysRevB.30.5596

939 Wood, B.J., Blundy, J.D., 2014. Trace element partitioning: the influences of ionic radius,  
940 cation charge, pressure, and temperature, in: Holland, H., Turekian, K. (Eds.), *Treatise*  
941 *on Geochemistry*: second edition. Elsevier Ltd., pp. 421–448. doi:10.1016/B978-0-08-  
942 095975-7.00209-6

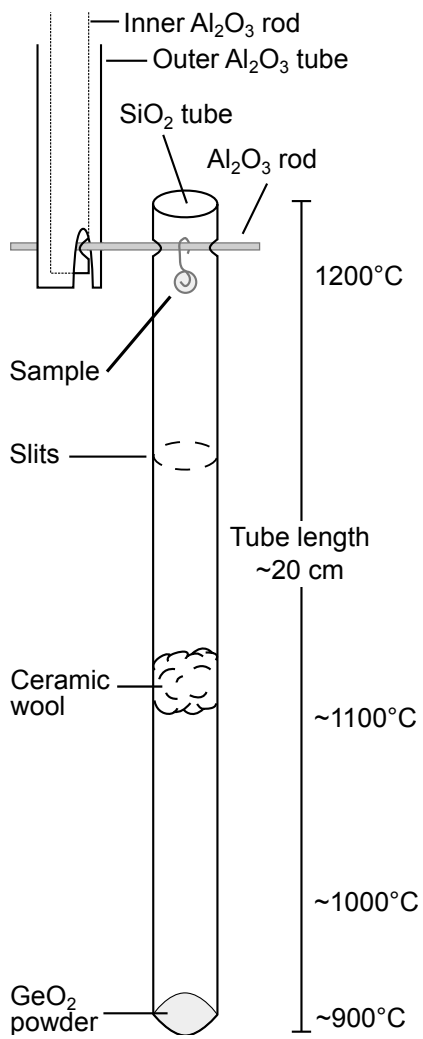
943 Wood, B.J., Walter, M.J., Wade, J., 2006. Accretion of the Earth and segregation of its core.  
944 *Nature* 441, 825–833. doi:10.1038/nature04763

945

946 **Figures**

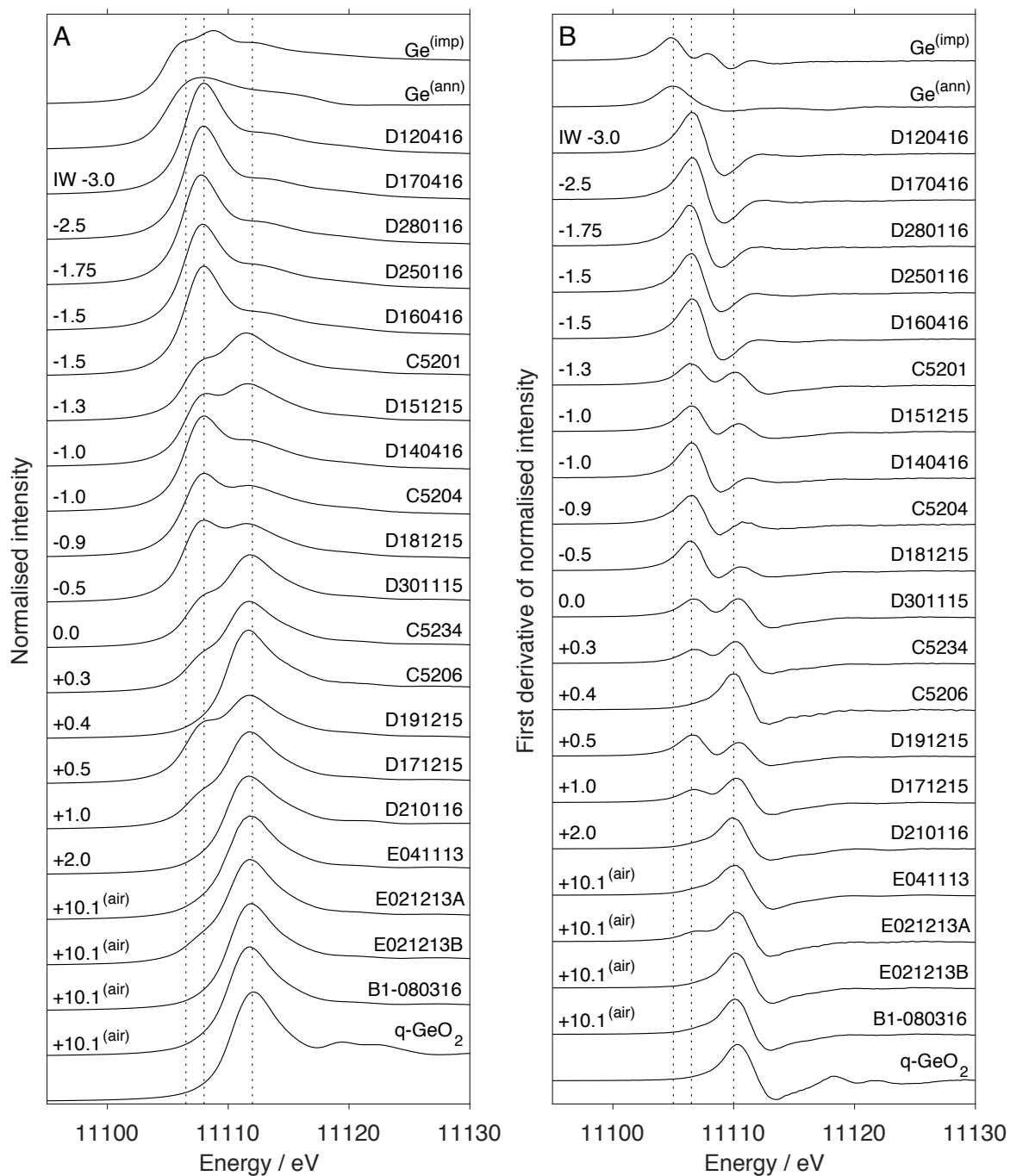


947  
 948 Figure 1. The  $fO_2$  ranges investigated, and Ge valence states determined by seven previous studies.  
 949 'S 89' = Schmitt et al., (1989), 1 atm, 1300–1600 °C. 'C 99' = Capobianco et al. (1999), 1 atm, 1260  
 950 °C. 'K 11' = Kegler and Holzheid (2011), 0.5 GPa, 1350 °C. 'S 11' = Siebert et al. (2011), 3 GPa,  
 951 1850–2200 °C. 'R 17' = Righter et al. (2017), 1 GPa, 1500–1900 °C. 'S 17' = Steenstra et al. (2017),  
 952 1.5 GPa, 1410–1610 °C. 'V 18' = Vogel et al. (2018), 11 GPa, 2310–2380 °C. The vertical grey line  
 953 indicates the IW buffer.



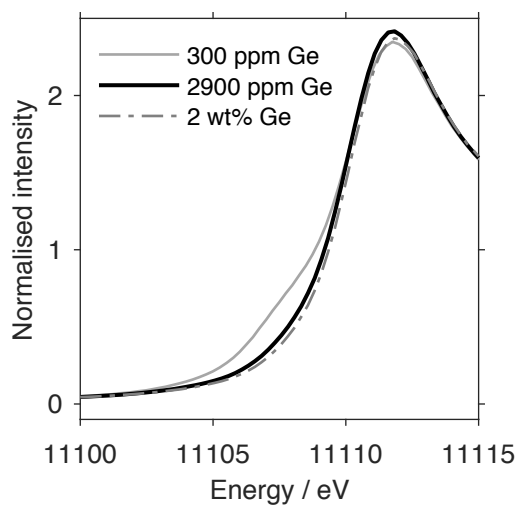
954  
 955  
 956

Figure 2. Experimental assembly used for ambient-pressure experiments at low  $f\text{O}_2$ .



957

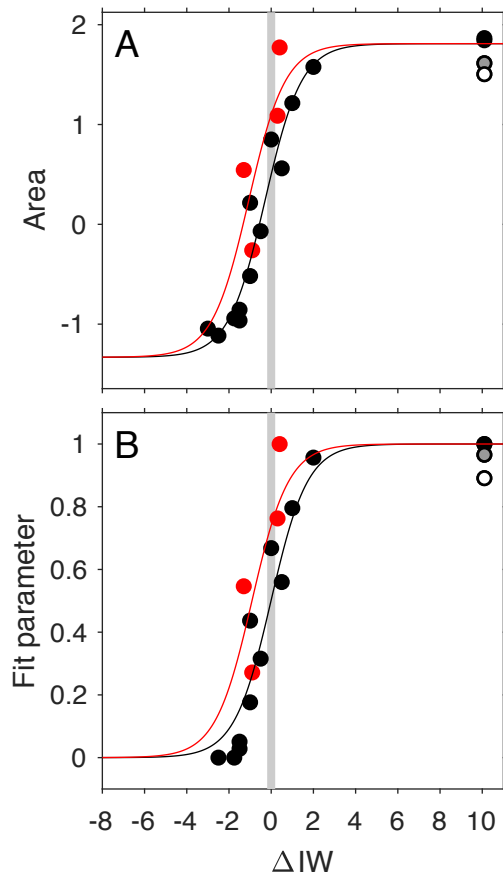
958 Figure 3. Ge K-edge (A) XANES and (B) first derivative of spectra of standards and glasses labelled  
 959 with the  $fO_2$  of equilibration (relative to IW). Spectra are offset for clarity and vertical dashed lines are  
 960 guides to the eye, plotted at 11106.5 eV, 11108.0 eV and 11112.0 eV in (A), and at 11105.0, 11106.5  
 961 and 11110.0 in (B).



962

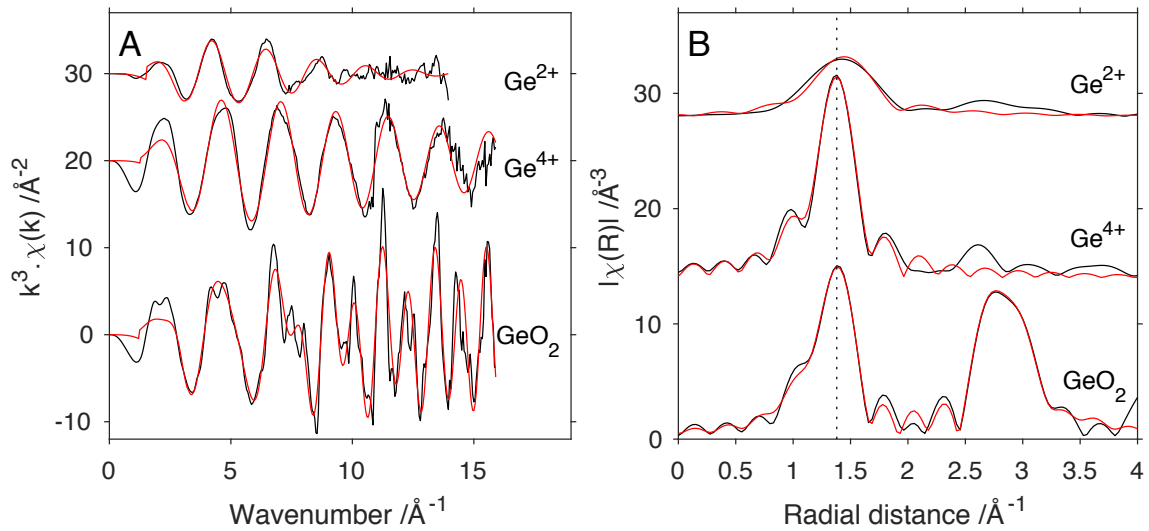
963 Figure 4. Ge K-edge XANES spectra of glass composition CMAS7G containing different  
964 concentrations of Ge (E021213A, 300 ppm; B1-080316, 2900 ppm; E021213B; 2 wt%).

965



966

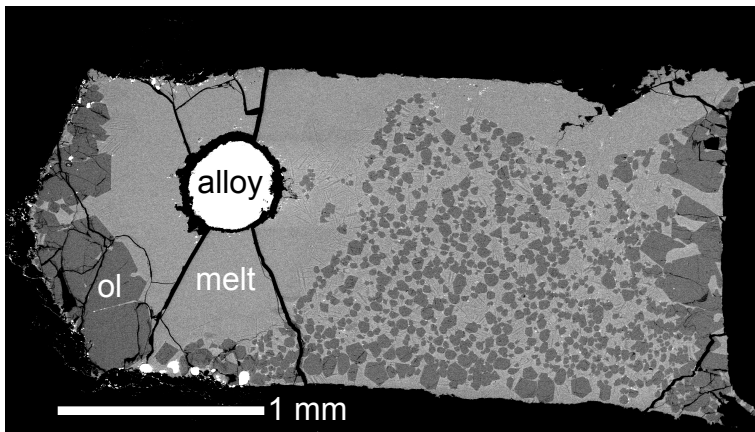
967 Figure 5. Representative results from the ‘spectral features’ and ‘linear combination fitting’  
 968 approaches to quantifying the spectra. (A) Area under the derivative spectrum from 11108 and 11112  
 969 eV (the ‘Ge<sup>4+</sup> peak’) against log $f_{\text{O}_2}$  relative to IW. (B) Fit parameters obtained from linear  
 970 combination fits using end-members B1-080316 (‘Ge<sup>4+</sup>’) and D120416 (‘Ge<sup>2+</sup>’). Filled black circles  
 971 represent samples made at ambient pressure and filled red circles represent samples made at 1 GPa.  
 972 The black and red curves are fits of Equation 6 (in A) or Equation 5 (in B) to the ambient-pressure  
 973 data and high-pressure data, respectively. Two data points were omitted from these fits (see text,  
 974 Section 3.3.1): samples E021213A (white circle) and E041113 (grey circle). Grey vertical bar shows  
 975 the log $f_{\text{O}_2}$  of the IW buffer.  
 976



977  
978  
979  
980  
981

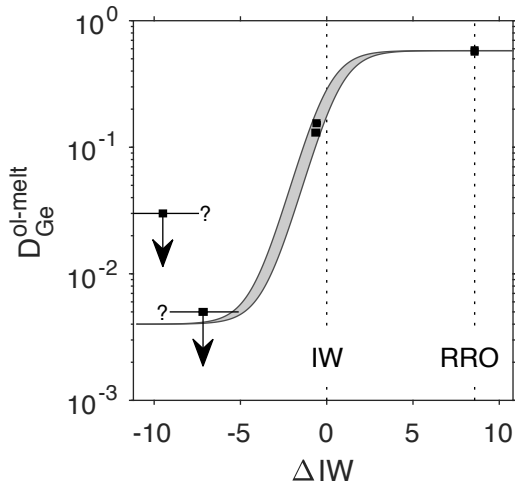
Figure 6. (A) Ge K-edge EXAFS spectra and (B) the Fourier transforms of the EXAFS spectra of  $\text{Ge}^{2+}$  (D120416) and  $\text{Ge}^{4+}$  (E041113) in glasses, and q- $\text{GeO}_2$ . Black curves are the spectra and red curves are fits to the spectra. The dashed line in (B) is a guide to the eye.

982



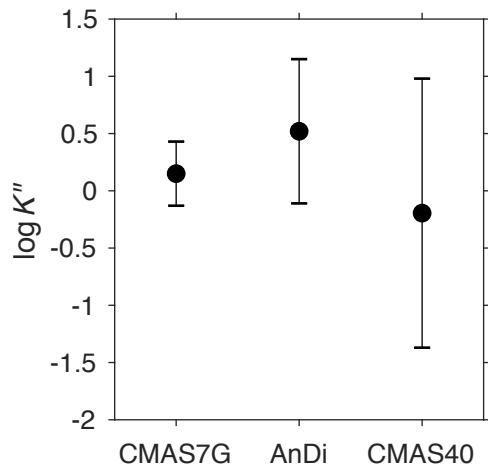
983

984 Figure 7. Backscattered electron image of sample D2357 (1500°C, 1 GPa, IW -7.2), showing metal  
985 alloy, olivine crystals (ol; dark grey) and silicate glass quenched from melt (light grey) in a graphite  
986 capsule (black).



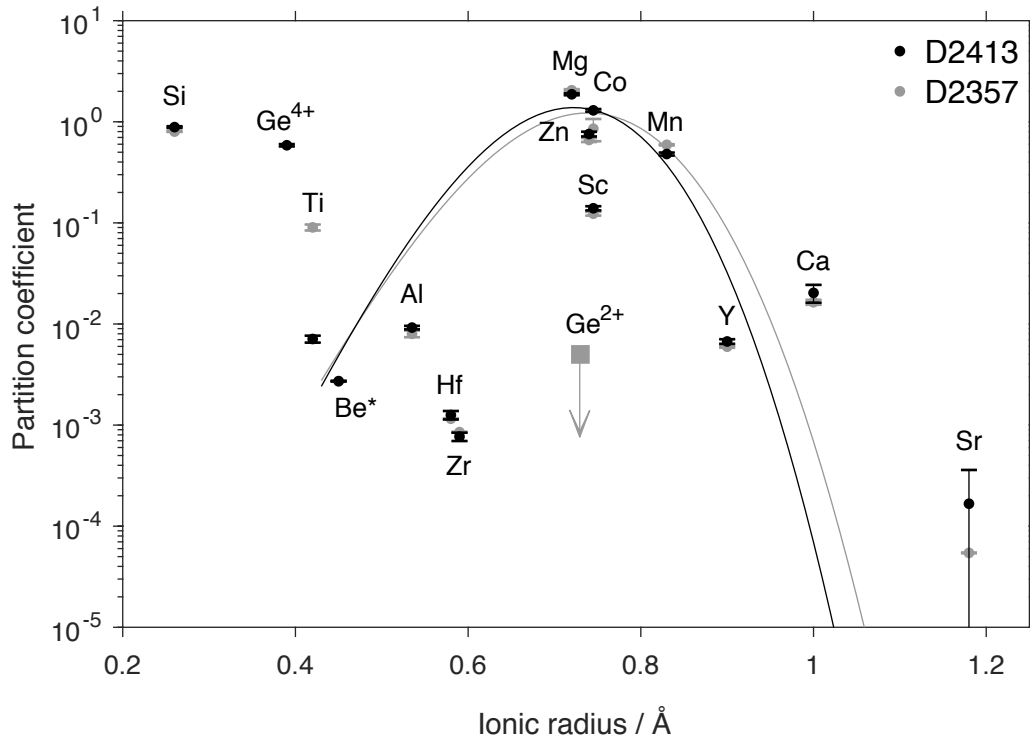
987

988 Figure 8. Partition coefficients of Ge between olivine and melt as function of  $\log fO_2$  relative to IW  
 989 (errors are smaller than the sizes of the symbols). Downward pointing arrows indicate maximum  
 990 partition coefficients, based on the LA-ICPMS detection limit, and the thin horizontal black lines on  
 991 these data points extend the error bars to an arbitrary  $\pm 2$  log units, in light of the uncertainties on the  
 992  $fO_2$  calculation (see text, Section 3.2). The wide grey curve shows the range of sigmoids that can be  
 993 fit to these partitioning data using Equation 8.



994

995 Figure 9. The  $\log K'$  values obtained from the three compositions used in this study. CMAS7G  
 996 experiments were performed at 1 atm and 1200 °C; AnDi and CMAS40 experiments were performed  
 997 at 1 GPa and 1500 °C.  
 998



999  
 1000  
 1001  
 1002  
 1003  
 1004  
 1005  
 1006  
 1007

Figure 10. Partition coefficients of elements in samples prepared at IW +8.6 (black; sample D2413) and IW -7.2 (grey; sample D2357) plotted against ionic radii. The black and grey curves show fits to a lattice strain model (see Equation S1, Table S7) for the 2+ cations in the two samples. The square with the downward pointing arrow marks the maximum partition coefficient of  $Ge^{2+}$  in D2357 at the ionic radius of  $Ge^{2+}$  in 6-fold coordination from Shannon (1976).

## 1008 **Supplementary Material**

### 1009 **S1. Nominal compositions of starting materials**

1010 Table S1. Nominal major-element concentrations (wt%) of starting materials.

	CMAS7G	AnDi	CMAS40 1011
SiO <sub>2</sub>	58.78	50.33	48.60
Al <sub>2</sub> O <sub>3</sub>	12.61	15.91	6.70
MgO	2.38	12.49	41.50
CaO	25.23	15.71	3.20

1012

### 1013 **S2. XAS methods**

1014 The spectrum of Ge in SiO<sub>2</sub> (implanted) was recorded in a previous experiment conducted by  
1015 the authors on the same beamline. The beamline setup was the same, however, there were  
1016 minor differences in count rates and step sizes. Firstly, the count rate was lower – maintained  
1017 between 13,500 s<sup>-1</sup> and 16,700 s<sup>-1</sup>. Secondly, the step sizes used were subtly different. For  
1018 XANES spectra, step sizes of 10 eV, 0.2 eV and 0.1 Å<sup>-1</sup> (to k=10) were used for the pre-edge,  
1019 edge and post-edge respectively. For EXAFS spectra, the step sizes were 10 eV, 0.4 eV and  
1020 0.05 Å<sup>-1</sup> (to k=16) respectively. By comparing four spectra that were acquired during both  
1021 experimental sessions, a systematic shift in edge energy and height of the white line was  
1022 observed. To account for this, the spectrum of Ge in SiO<sub>2</sub> (implanted) was shifted in energy  
1023 by -0.37 eV. The height of the white line was not corrected for.

1024

1025 **S3. Glass compositions**

1026 Table S2. Major element compositions for selected ambient-pressure glasses, determined by EDS  
 1027 using a FE-SEM.

	D171215	sd	D191215	sd	D21/01/16	sd	D301115	sd
n	3		3		3		2	
MgO	2.41	0.14	2.43	0.02	2.53	0.16	2.40	0.08
Al <sub>2</sub> O <sub>3</sub>	12.29	0.68	11.73	0.31	12.42	0.36	12.17	0.09
SiO <sub>2</sub>	58.67	1.09	58.50	0.63	57.95	0.67	58.57	0.95
P <sub>2</sub> O <sub>5</sub>	0.08	0.14	0.63	0.56	0.00	0.00	0.38	0.13
CaO	24.27	0.83	24.55	0.27	24.64	0.56	24.75	0.62
GeO <sub>2</sub>	0.98	0.19	0.45	0.04	1.97	0.12	0.48	0.09
Total	98.70	0.61	98.28	0.24	99.51	0.16	98.75	0.11

	E021213A	sd	E021213B	sd
n	3		3	
MgO	2.34	0.02	2.33	0.02
Al <sub>2</sub> O <sub>3</sub>	12.47	0.29	11.97	0.07
SiO <sub>2</sub>	60.91	0.40	58.06	0.54
CaO	23.76	0.17	22.09	0.20
GeO <sub>2</sub>			3.07	0.04
Total	99.48	0.02	97.52	0.52

1028 *n* = number of analyses.

1029

1030 Table S3. Major element compositions for glasses prepared at 1 GPa, determined by EPMA.

	C5201	sd	C5204	sd	C5206	sd	C5234	sd
<i>n</i>	12		12		14		9	
MgO	11.8	0.1	10	0.2	10.7	0.1	10.3	0.2
Al <sub>2</sub> O <sub>3</sub>	14	0.2	14.5	0.2	13.9	0.2	14.1	0.2
SiO <sub>2</sub>	51	0.5	51.7	0.3	45.1	0.3	46.9	0.6
CaO	22.1	0.2	22.6	0.1	21.9	0.2	22.2	0.2
GeO <sub>2</sub>	0.29	0.07	0.96	0.05	5.6	0.1	3.9	0.2
NiO	0.03	0.02	0.01	0.02	0	0.02	0.01	0.02
CoO	bdl		0.53	0.03	2.53	0.03	2.12	0.05
Total	99.3	0.7	100.4	0.6	99.8	0.5	99.5	0.9

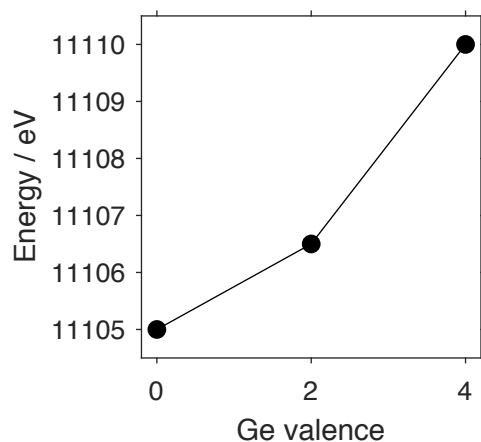
1031 *n* = number of analyses.

1032

1033

1034 S4. XAS results

1035



1036  
1037  
1038  
1039

Figure S1. The Ge XANES edge energy, defined as the first maximum in the derivative spectrum, as a function of the Ge valence state.

1040

Table S4. The results of six methods of quantifying the spectra based on spectral features.

Sample	$\Delta I W$	Spectral feature*					
		A	B	C	D	E	F
B1-080316	+10.1	0.56	2.39	2.53	9.81	0.44	1.84
E021213B	+10.1	0.49	2.36	2.25	9.65	0.38	1.87
E021213A	+10.1	0.83	2.30	3.14	10.01	0.69	1.50
E041113	+10.1	0.65	2.28	2.57	9.12	0.46	1.61
D210116	+2.0	0.59	2.14	2.66	9.14	0.46	1.58
D171215	+1.0	0.94	2.14	3.81	9.00	0.80	1.21
D191215	+0.5	1.41	1.95	5.38	8.42	1.26	0.56
C5206	+0.4	0.60	2.33	2.77	9.82	0.47	1.77
C5234	+0.3	0.95	2.03	3.73	8.61	0.81	1.09
D301115	0.0	1.22	2.05	4.72	8.73	1.07	0.85
D181215	-0.5	1.82	1.74	7.08	7.69	1.69	-0.07
C5204	-0.9	1.86	1.59	7.03	7.19	1.71	-0.26
D140416	-1.0	2.13	1.59	7.83	7.28	1.98	-0.52
D151215	-1.0	1.63	1.83	6.11	8.10	1.48	0.22
C5201	-1.3	1.40	1.92	5.45	8.40	1.26	0.54
D160416	-1.5	2.43	1.44	8.80	6.81	2.27	-0.96
D250116	-1.5	2.36	1.49	8.56	6.96	2.20	-0.86
D280116	-1.8	2.39	1.43	9.05	6.72	2.26	-0.94
D170416	-2.5	2.52	1.39	9.07	6.65	2.36	-1.11
D120416	-3.0	2.46	1.40	8.97	6.67	2.30	-1.04

1041  
1042  
1043  
1044  
1045

\*Columns A–F refer to the following spectral features: (A) the intensity at 11108 eV, (B) the intensity at 11112 eV, (C) the area under the spectrum between 11105 and 11110 eV, (D) the area under the spectrum between 11110 and 11115 eV, (E) the area under the derivative spectrum between 11102 and 11108 eV, and (F) the area under the derivative spectrum between 11108 and 11112 eV.



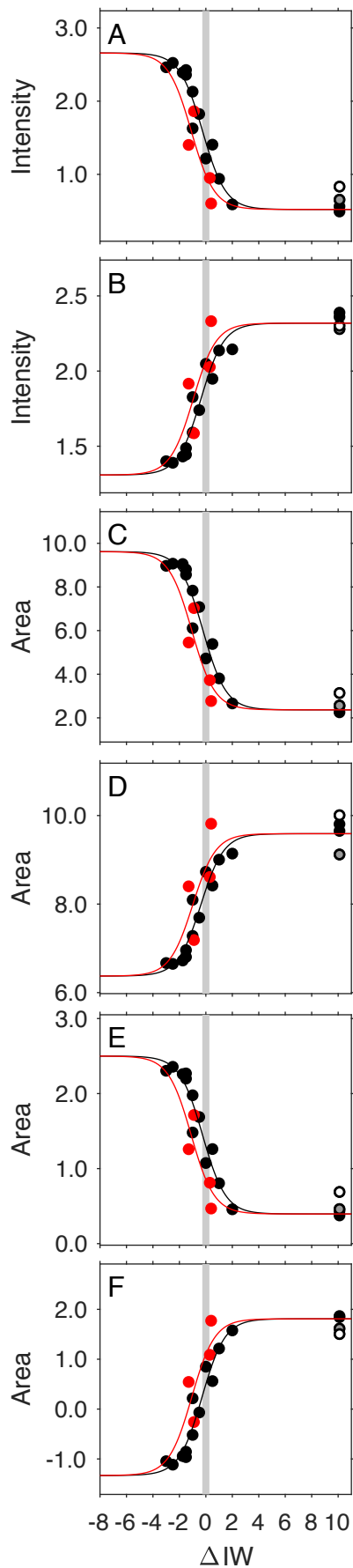
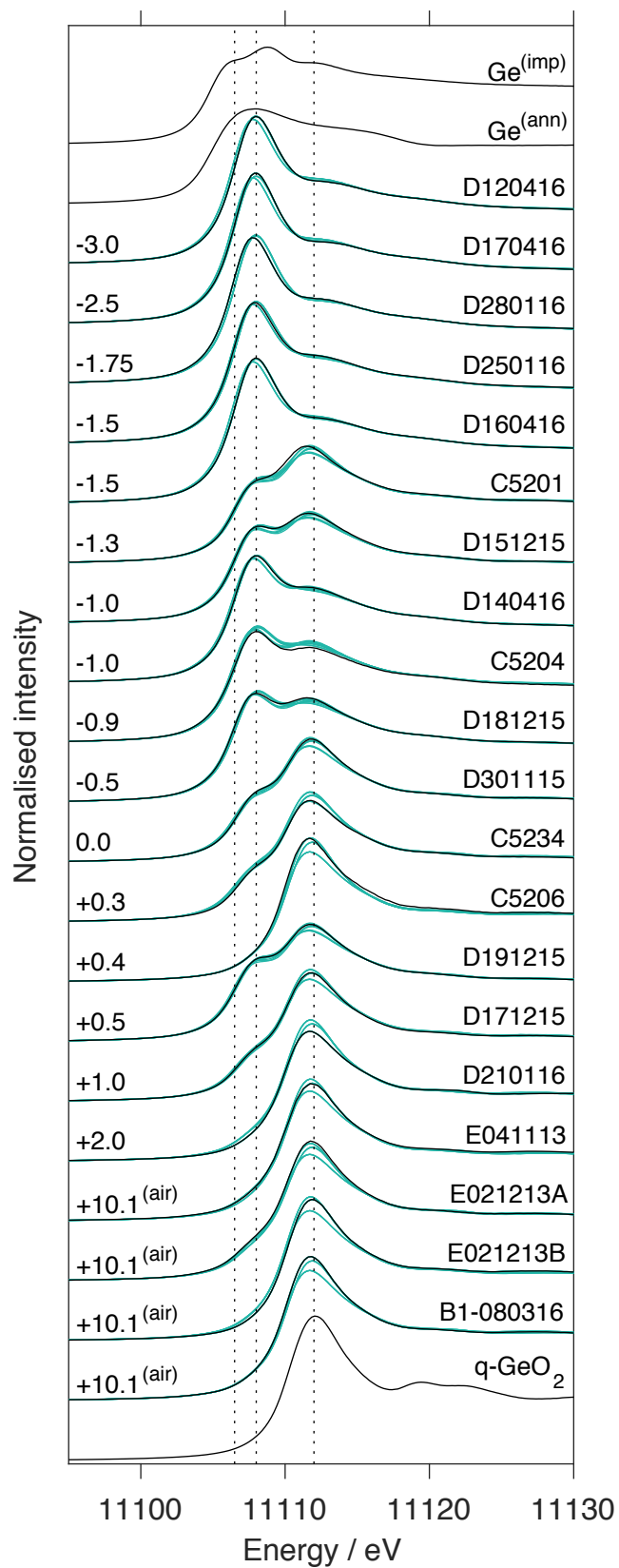


Figure S2. Results of six methods of parameterising the spectra. Panels A–F show results based on the following methods: (A) the intensity at 11108 eV, (B) the intensity at 11112 eV, (C) the area under the spectrum between 11105 and 11110 eV, (D) the area under the spectrum between 11110 and 11115 eV, (E) the area under the derivative spectrum between 11102 and 11108 eV, and (F) the area under the derivative spectrum between 11108 and 11112 eV. Filled black circles represent samples made at ambient pressure and filled red circles represent samples made at 1 GPa. The black and red curves are fits of Equation 6 to the ambient-pressure data and high-pressure data, respectively. Two data points were omitted from these fits (see text, Section 3.3.1): samples E021213A (white circle) and E041113 (grey circle).  $2\sigma$  uncertainties resulting from noise in the spectra are smaller than the size of the symbols. The grey vertical bar indicates the  $\log f_{O_2}$  of the IW buffer.



1048  
1049  
1050

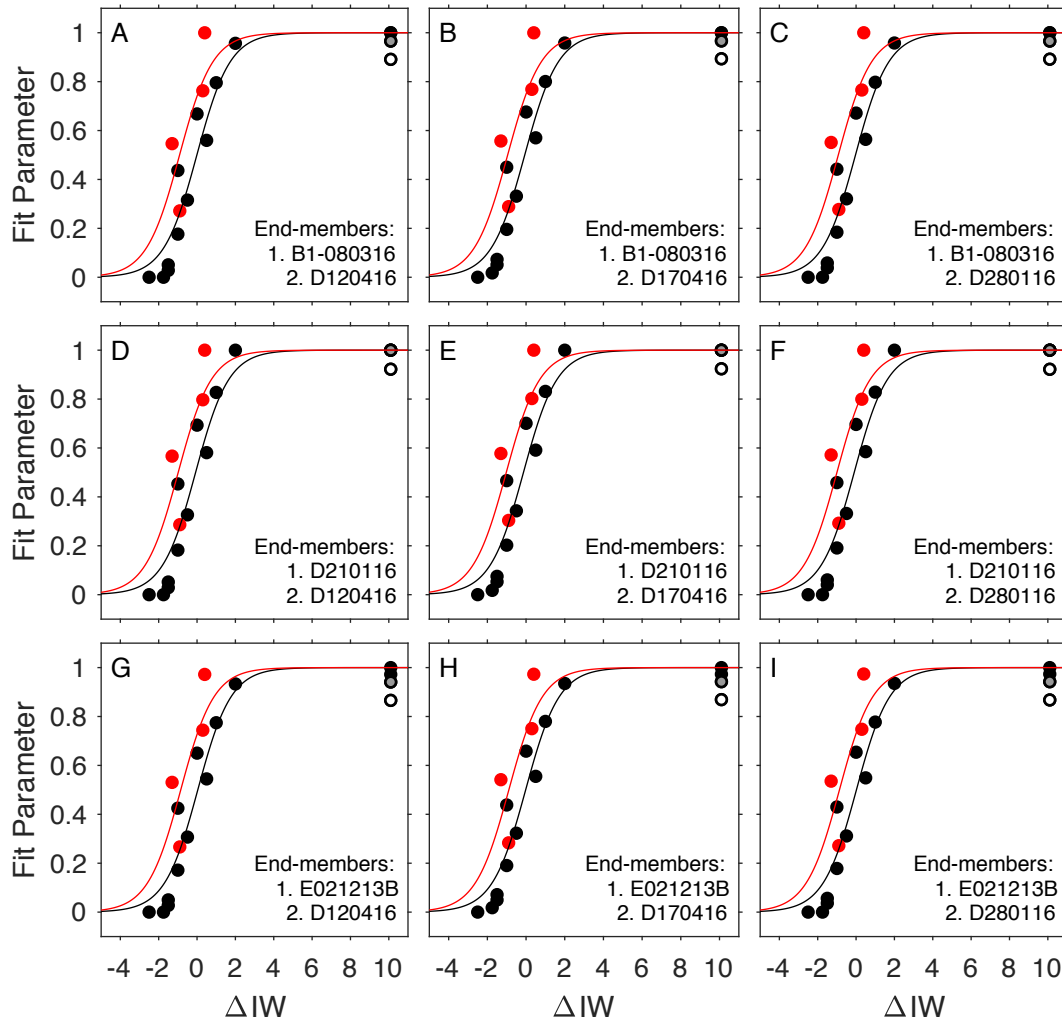
Figure S3. Linear combination fits (green) to spectra (black).

1051 Table S5. The results of nine linear combination fits between different end-members.

Sample	$\Delta IW$	Fit parameter, based on end-member combination*								
		A	B	C	D	E	F	G	H	I
B1-080316	+10.1	1.00	1.00	1.00	1.00	1.00	1.00	0.97	0.97	0.97
E021213A	+10.1	0.89	0.89	0.89	0.92	0.92	0.92	0.87	0.87	0.87
E021213B	+10.1	1.00	1.00	1.00	1.00	1.00	1.00	1.00	1.00	1.00
E041113	+10.1	0.97	0.97	0.97	1.00	1.00	1.00	0.94	0.94	0.94
D210116	+2.0	0.96	0.96	0.96	1.00	1.00	1.00	0.93	0.94	0.94
D171215	+1.0	0.80	0.80	0.80	0.83	0.83	0.83	0.77	0.78	0.78
D191215	+0.5	0.56	0.57	0.56	0.58	0.59	0.58	0.54	0.56	0.55
C5206	+0.4	1.00	1.00	1.00	1.00	1.00	1.00	0.97	0.97	0.97
C5234	+0.3	0.76	0.77	0.77	0.80	0.80	0.80	0.74	0.75	0.75
D301115	0.0	0.67	0.68	0.67	0.69	0.70	0.70	0.65	0.66	0.65
D181215	-0.5	0.32	0.33	0.32	0.33	0.34	0.33	0.31	0.32	0.31
C5204	-0.9	0.27	0.29	0.28	0.29	0.30	0.29	0.27	0.28	0.27
D140416	-1.0	0.18	0.20	0.18	0.18	0.20	0.19	0.17	0.19	0.18
D151215	-1.0	0.44	0.45	0.44	0.45	0.47	0.46	0.42	0.44	0.43
C5201	-1.3	0.55	0.56	0.55	0.57	0.58	0.57	0.53	0.54	0.54
D160416	-1.5	0.03	0.05	0.04	0.03	0.05	0.04	0.03	0.05	0.04
D250116	-1.5	0.05	0.07	0.06	0.05	0.08	0.06	0.05	0.07	0.06
D280116	-1.8	0.00	0.02	0.00	0.00	0.02	0.00	0.00	0.02	0.00
D170416	-2.5	0.00	0.00	0.00	0.00	0.00	0.00	0.00	0.00	0.00
D120416	-3.0	0.00	0.02	0.01	0.00	0.02	0.01	0.00	0.02	0.01

1052 \*Columns A–I refer to the following combinations of end-members: (A) B1-080316 & D120416, (B)  
 1053 B1-080316 & D170416, (C) B1-080316 & D280116, (D) D210116 & D120416, (E) D210116 &  
 1054 D170416, (F) D210116 & D280116, (G) E021213B & D120416, (H) E021213B & D170416, (I)  
 1055 E021213B & D280116.

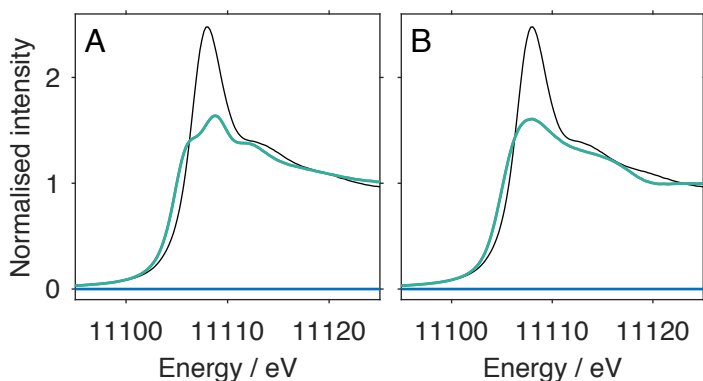
1056  
 1057  
 1058  
 1059



1060  
 1061  
 1062  
 1063  
 1064  
 1065  
 1066  
 1067

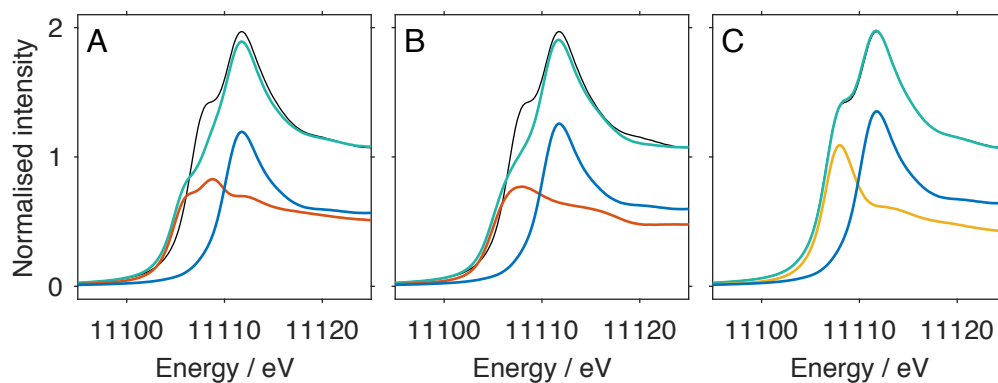
Figure S4. Results of linear combination fitting of different end-members (specified on each panel) to the XANES spectra. Filled black circles represent samples made at ambient pressure and filled red circles represent samples made at 1 GPa. The black and red curves show fits to Equation 5 (see main text). Two data points were omitted from these fits (see text, Section 3.3.1): samples E021213A (white circle) and E041113 (grey circle). Confidence intervals on the fitted parameters are smaller than the size of the symbols.

1068



1069  
1070  
1071  
1072  
1073  
1074  
1075

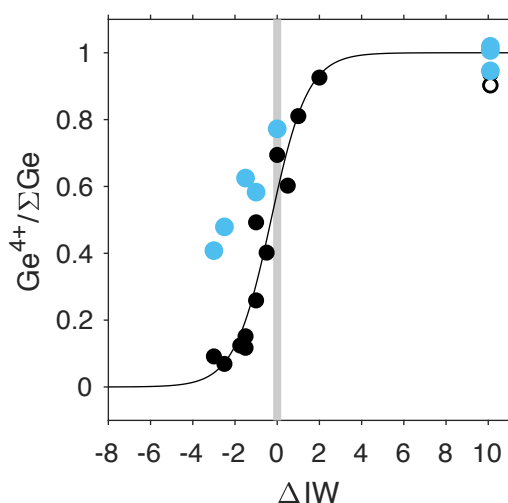
Figure S5. Examples of linear combination fits (green) the spectrum of a sample prepared at IW -3 (black), using different end-members. The  $\text{Ge}^{4+}$  end-member is B1-080316 (blue), and the 'reduced species' end-members are (A)  $\text{Ge}^0(\text{imp})$  and (B)  $\text{Ge}^0(\text{ann})$ . The best fit in both cases had a  $\text{Ge}^{4+}$  component of 0% (flat blue line), and a  $\text{Ge}^0$  component of 100% (green curve), but in both cases the fit is poor.



1076  
1077  
1078  
1079  
1080  
1081  
1082

Figure S6. Examples of linear combination fits (green) the spectrum of a sample prepared at IW +0.5 (black), using different end-members. The two end-member components are plotted as blue, red and yellow curves. The  $\text{Ge}^{4+}$  end-member is B1-080316 (blue), and the 'reduced species' end-members are (A)  $\text{Ge}^0(\text{imp})$  (red), (B)  $\text{Ge}^0(\text{ann})$  (red), and (C) a glass prepared at IW -3 (yellow). The fits using the  $\text{Ge}^0$  spectra (A, B) are poor compared to the fit using the spectrum assigned to  $\text{Ge}^{2+}$  (C).

1083  
1084  
1085



1086  
1087  
1088  
1089  
1090  
1091  
1092  
1093  
1094  
1095  
1096  
1097

Figure S7.  $\text{Ge}^{4+}/\Sigma\text{Ge}$  calculated by normalising the results Figure 5A onto a scale of 0 to 1. Grey line indicates the IW buffer. Filled black circles represent samples made at ambient pressure. White circle is sample E021213A. Blue circles show the result of ‘correcting’ the data based on the assumption that all  $\text{Fe}^{2+}$  in the sample reacted upon quenching to form  $\text{Ge}^{2+}$  (Table S6). This component of  $\text{Ge}^{2+}$  hypothetically produced on quenching is then subtracted from the amount calculated to be in the sample based on the spectral features. Only samples for which Fe was measured using LA-ICPMS are ‘corrected’. When the data are ‘corrected’ in this manner, the sigmoidal trend does not follow the expected slope (black curve).

Table S6. Fe and Ge contents and valence states used to ‘correct’ data in Figure S7.

Sample name	$\Delta\text{IW}$	$\Sigma\text{Fe}$ (at.ppm) <sup>1</sup>	$\text{Fe}^{2+}$ (at.ppm) <sup>2</sup>	$\Sigma\text{Ge}$ (at.ppm) <sup>1</sup>	$\text{Ge}^{2+}$ produced from $\text{Fe}^{2+}$ (at.ppm) <sup>3</sup>
E021213B	+10.1	431 (35)	50 (4)	17459 (252)	25 (2)
E041113	+10.1	255 (13)	29 (2)	1791 (85)	15 (1)
E021213A	+10.1	464 (36)	53 (4)	256 (85)	27 (2)
D301115	+0.0	379 (21)	370 (20)	2371 (825)	185 (10)
D140416	-1.0	398 (5)	392 (5)	606 (353)	196 (2)
D160416	-1.5	361 (5)	357 (5)	352 (70)	179 (2)
D170416	-2.5	354 (8)	353 (8)	430 (79)	176 (4)
D120416	-3.0	352 (6)	350 (6)	553 (71)	175 (3)
Sample name	$\Delta\text{IW}$	$\text{Ge}^{4+}/\Sigma\text{Ge}$ ratio <sup>4</sup>	$\text{Ge}^{2+}$ (at.ppm) <sup>4</sup>	“Corrected” $\text{Ge}^{2+}$ (at.ppm) <sup>5</sup>	“Corrected” $\text{Ge}^{4+}/\Sigma\text{Ge}$
E021213B	+10.1	1.02	-311	-336	1.02
E041113	+10.1	0.94	112	97	0.95
E021213A	+10.1	0.90	25	-2	1.01
D301115	+0.0	0.69	725	540	0.77
D140416	-1.0	0.26	449	253	0.58
D160416	-1.5	0.12	311	132	0.63
D170416	-2.5	0.07	400	224	0.48
D120416	-3.0	0.09	502	327	0.41

1098  
1099  
1100

<sup>1</sup>From LA-ICPMS measurements. <sup>2</sup>Based on parameterisation of  $\text{Fe}^{3+}/\text{Fe}^{2+}$  of O’Neill et al. (2018), their equation 9b. <sup>3</sup>Hypothetical amount of  $\text{Ge}^{2+}$  produced if the electron-exchange reaction went to completion. <sup>4</sup>Calculated from spectral features. <sup>5</sup>Calculated as  $\text{Ge}^{2+}_{\text{total}} - \text{Ge}^{2+}_{\text{produced-from-Fe}^{2+}}$ .



1102

### 1103 5.1 S4. Partitioning results

1104 Partition coefficients were fit to a lattice strain model (Blundy and Wood, 1994; Brice, 1975):

$$1105 \quad D_i = D_o * \exp\left(\frac{-4\pi E_s N_A \left(\frac{r_o}{2} (r_o - r_i)^2 + \frac{1}{3} (r_o - r_i)^3\right)}{RT}\right)$$

1106

Equation S1

1107

1108 where  $D_i$  is the partition coefficient as a function of ionic radius  $r_i$ ,  $N_A$  is Avogadro's number,

1109  $R$  is the ideal gas constant,  $T$  is temperature in K,  $D_o$  is the partition coefficient of a fictional

1110 cation with the 'ideal' radius  $r_o$ , and  $E_s$  is the Young's modulus for the crystallographic site.

1111 Fit parameters are given in Table S7.

1112

1113 Table S7. Fit parameters for lattice strain model (2+ cations in the octahedral site of olivine). Numbers

1114 in parentheses are  $\pm 95\%$  confidence intervals on the last digit.

1115

	D2413	D2357
$D_o$	1.4 (8)	1.2 (10)
$E_s$	550 (451)	467 (491)
$r_o$	0.72 (7)	0.74 (8)

1116